Development of an Electronic Nose for Detection of Volatile Organic Compounds Based on Nanoporous Microcantilevers by Using Photothermal Spectroscopy

by

Inseok Chae

A thesis submitted in partial fulfillment of the requirements for the degree of

Master of Science

in

Chemical Engineering

Department of Chemical and Materials Engineering

University of Alberta

Abstract

An electronic nose for identification and quantification of volatile organic compounds (VOCs) mixtures was developed using a nanopore-enhanced photothermal cantilever deflection spectroscopy (PCDS). PCDS provides highly selective detection of vapor mixtures of VOCs from specific molecular vibrations in the mid IR region. Nanoporous anodic aluminum oxide (AAO) microcantilevers, fabricated through the self-ordering anodization and simple photolithography, were exploited with PCDS in order to increase the sensitivity. AAO microcantilevers were optimized by tuning the diameter of nanopores in order to enhance the thermomechanical sensitivity and increase the surface area. The thermomechanical sensitivity of a bilayer AAO microcantilever with 60 nm of pore diameter was estimated ~1 μm/K and was found to be much superior to that of plain Si microcantilever due to its nanoporous structure. The adsorbed molecules from vapor mixtures on AAO microcantilevers in humid condition were fully recognized and quantified by measuring the peak amplitudes in PCDS and the resonance frequency shifts of AAO microcantilevers.

Keywords: electronic nose, VOCs, AAO, PCDS, thermomechanical sensitivity

Preface

This thesis is an original work done by Inseok Chae. No part of this thesis has been previously published yet, but will be submitted to a scientific journal when the manuscript is ready. The experimental set up and fabrication process referred in chapter 2 were designed by Inseok Chae and Dr. Dongkyu Lee, with the guidance of Prof. Thomas Thundat. The data analysis in chapter 3 is Inseok Chae's original work, as well as the literature review in chapter 1.

Dedication

This thesis is dedicated to my father, mother and brother for their love, endless support and encouragement. Also, I would like to dedicate this thesis to my great friends at the University of Alberta including Amrith Kumar and Andrew Jo.

Acknowledgement

Throughout my whole MSc program, many of our Nano Interfaces and Molecular Engineering (NIME) group members have helped me. I would like to thank all of them. Without their help, the completion of this thesis was impossible.

First, I would like to thank my supervisor, Prof. Thomas Thundat for providing great research advices and opportunities during the whole MSc program. He has disciplined me to be a strong leader and taught me how to be a professional researcher. His heart-warming guidance gave the best resource to successfully complete my MSc program.

Also, I would like to show my appreciation towards Dr. Dongkyu Lee for teaching me how to do independent research from very basic to high level skills. He really inspired me to work hard and developed my creative thinking during the entire MSc program. I will remember his hands-on training forever.

Lastly, I am greatly thankful to all my NIME group members including Prof. Seonghwan Kim, Dr. Ravi Gaikwad, Dr. Faheem Khan and Dr. Xunchen Liu. While working with them in the National Institute for Nanotechnology research labs at the University of Alberta, I really enjoyed doing research for the whole time of my MSc program.

Table of Contents

List of Tables

List of Figures

Abbreviations

AAO	Anodic aluminum oxide
AAO35	AAO microcantilever with 35 nm pore diameter
AAO50	AAO microcantilever with 50 nm pore diameter
AAO60	AAO microcantilever with 60 nm pore diameter
AAO70	AAO microcantilever with 70 nm pore diameter
AFM	Atomic force microscope
DI water	Deionized water
D_{int}	Interpore distance
D_p	Pore diameter
E-nose	Electronic nose
FTIR	Fourier transform infrared spectroscopy
GC	Gas chromatography
Hz	Hertz
IR	Infrared
IUPAC	International union of pure and applied chemistry
LOD	Limit of detection
M	Molar concentration
MFCs	Mass flow controllers
MS	Mass chromatography

ms	Milliseconds
N_2	Nitrogen
nm	Nanometers
PCDS	Photothermal cantilever deflection spectroscopy
pg	Picogram (10^{-12})
ppb	Parts-per-billion
ppm	Parts-per-million
ppt	Parts-per-trillion
ppth	Parts-per-thousand
PR	Photo resist
PSD	Position sensitive detector
QCL	Quantum cascade laser
QCM	Quartz crystal microbalance
RH	Relative humidity
s	Seconds
sccm	Standard cubic centimeters per minute
SEM	Scanning electron microscope
Si	Silicon
UV	Ultra violet light
V	Voltages
VOCs	Volatile organic compounds
μm	Micrometers

Chapter 1. Introduction

Outline: This chapter presents the motivation to work on this MSc thesis. A brief introduction to the project and prior research, which are relevant to this project, is described. The goal of this project is also explained.

1.1 Chemical sensor

According to the International Union of Pure and Applied Chemistry (IUPAC), a chemical sensor is, "a device that transforms chemical information, ranging from the concentration of a specific sample component to total composition analysis, into an analytically useful signal" [1]. Chemical sensors normally consist of a receptor and transducer, and are designed to detect a certain types of sample (Figure 1.1)[2] [3].

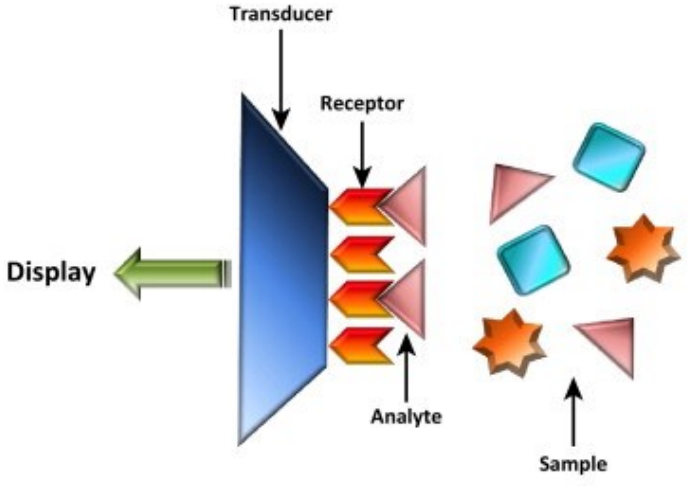

Figure 1.1. Schematic of a typical chemical sensor including a receptor and transducer[3]

Chemical information of compounds on a sensing surface is converted to an energy form in the receptor. This transformed energy from the receptor is again transformed into a readable signal in the transducer[1]. By analyzing the signal generated from the transducer, we can obtain the information of target samples. A sensor array is a group of sensors, which enables the systems to analyze multiple components as each sensor can generate independent sensing signals from target analytes in controlled operating conditions[4].

There are several characteristics to evaluate the performance of chemical sensors including sensitivity and selectivity. Sensitivity refers to a change of sensing signals according to the shift of analyte concentrations[5]. It is different from the limit of detection, which is the lowest concentration or smallest amount of target samples that a sensor can reliably detect. Selectivity of a sensor provides information of whether the sensor can respond and differentiate a certain component from other compounds[6]. It is also different from the limit of recognition, which is the lowest ratio of target analyte to other compounds that a sensor can recognize[7]. Another characteristic, which is important in evaluating the performance of chemical sensors is stability. It is a capability of sensors to produce consistent results preserving sensitivity and selectivity for a certain period of time[2]. Resolution, response time, portability and regeneration are also taken into account to characterize chemical sensors.

Chemical sensors have numerous applications including bio-medical devices, industrial food analysis, environmental control, human health monitoring etc[8]. We can use chemical sensors for the analysis of clinical samples such as blood, tissue and urine to detect human and animal diseases[9]. Especially, the importance of vapor phase assessment in the field of medical diagnosis has been emphasized by the development of a breath analysis with which we are able to detect human diseases from exhaled breaths[9–11]. In the agriculture and food industry, we can detect crop

diseases and identify virus penetrations and food qualities by analyzing volatile organic compounds (VOCs) generated by plants and foods[12 13]. Chemical sensors play a significant role in environmental monitoring by measuring the concentrations of pollutants in air, water and soil[14 15]. Also, chemical sensors are used in process controls, industrial safety and military actions. To improve the performance of chemical sensors in these various fields, we need to enhance the characteristics of chemical sensors mentioned above.

1.2 Electronic nose

An electronic nose (e-nose) is one kind of chemical sensors, which attempts to emulate a human olfactory system by utilizing a sensor array combined with pattern recognition softwares[16–18]. In the human olfactory system, information of chemical compounds drawn to olfactory receptors is transformed to an electrical signal in neurons[19]. This electrical signal is transferred to a brain through olfactory nerves which is translated as the chemical information. The human olfactory system is very useful in recognizing the chemical compounds in a vapor phase; however, it has individual variations and it becomes insensitive when people are exposed to smells for a certain period of time[20]. Researchers have developed gas chromatography and mass spectrometry (GC/MS) to overcome these defects and obtain more consistent results[21 22]. These techniques have been widely used to quantify and qualify multiple chemical constituents in a vapor phase with high sensitivity and selectivity, but they have chronic problems such as an expensive operating cost, slow performance and bulky size. In order to overcome these limitations, researchers have been developing novel analytical gas sensing techniques referred to as e-nose for several decades. The basic principle of the e-nose is different from GC/MS in that it is cost-effective, portable and fast enough to show a real time performance[23].

In the e-nose system, odor molecules are drawn to sensor arrays through samplers such as a pre-concentrator or bubbler. Sensor arrays individually react to the drawn molecules and cause reversible physical or chemical changes on sensor substrates[24]. This changes the electrical properties at the receptor, and generates electrical signals in the transducer section[24]. The electrical signals from the transducer are conditioned and processed, and then identified through the pattern recognition system.

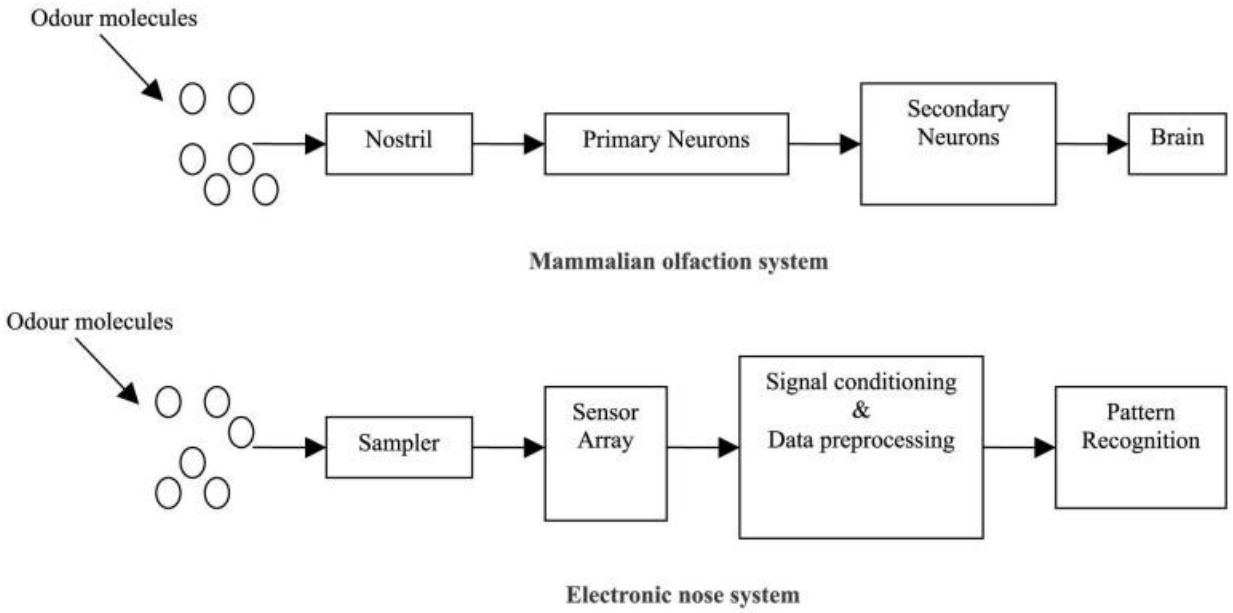

Figure 1.2. Comparison of the mammalian olfactory system and e-nose system[16]

By analyzing the electrical signals processed from e-nose system as shown in Figure 1.2, we can quantify and qualify the target samples.

There are dominantly three methods to analyze the electrical signals from an e-nose system; differential, relative and fractional methods[25].

E-nose signal analyzing methods	Equations
Differential	$y_s(t) = x_s(t) - x_s(0)$
Relative	$y_s(t) = \frac{x_s(t)}{x_s(0)}$
Fractional	$y_s(t) = \frac{x_s(t) - x_s(0)}{x_s(0)}$

Table 1.1. Three main methods to analyze a sensing response with respect to a baseline from e-nose[25].

Table 1.1 shows equations of the three dominant methods used. In a differential method, the baseline manipulated sensor response $y_s(t)$ is calculated by subtracting the baseline $x_s(0)$ from the sensor response $x_s(t)$. In a relative method, the sensor response $x_s(t)$ is divided by a baseline $x_s(0)$. The difference in the response $x_s(t)$ and baseline $x_s(0)$ is divided by the baseline in a fractional method. This method provides a normalized sensor response. E-nose devices generate different forms of electrical signals. Thus, we need to choose which method to use in order to get a proper sensor response depending on the form of electrical signals from e-nose.

There are three major types of chemicals sensors that have been implemented as e-nose; a conductivity sensor, piezoelectric sensor and an optical sensor[17 11 22 26]. A **conductivity sensor** utilizes conductivity changes of sensing materials when gas molecules are adsorbed on the

surface[27]. Conducting polymer composite sensors and metal oxide sensors are the examples of the conductivity sensor. In conducting polymer composite sensors, a conducting polymer such as a polypyrrole expands when certain vapor molecules permeate, and causes an increase in electrical resistance of the polymer. This is because of the reduction in the number of pathways for charge carriers following the polymer expansion[28]. Different polymers have different levels of the permeation to vapor molecules, and there are numerous conducting polymers applicable. Thus, we can selectively detect numerous vapor molecules by implementing various conducting polymers on sensor arrays. In most cases, the fractional baseline manipulation method is used in the data processing[28]. One of the main advantages of such sensors is that preparing conducting polymers and signal circuits to measure the resistance changes are relatively cheap and simple. In addition, conducting polymers can operate at room temperature without the need of external temperature control. The main drawback of conducting polymer composite sensors is that polymer composites age quickly, which disturbs the stability of the sensors. Additionally, the number of target molecules that can be detected with one conducting polymer sensor is limited because it is sensitive to only certain types of vapor molecules. Another disadvantage is that some organic molecules are insensitive to conducting polymer composites – i.e. trimethylamine (TMA)[16].

A **metal oxide sensor** also utilizes the conductivity changes of sensing materials when they are exposed to vapor molecules[16]. The conductance of the oxide layer changes due to an interaction with adsorbed vapor molecules on the surface. In *n*-type metal oxide sensors, oxygen in the air reacts with metal oxide surfaces such as zinc oxide or titanium dioxide and traps free electrons on sensing materials. This generates resistance changes on the reaction sites[25]. While, in *p*-type, oxidizing gases like O_2, NO_2 and Cl_2 react on metal oxide surfaces such as nickel oxide or cobalt oxide, and produce holes on sensing materials by removing electrons[25]. The main advantages of

metal oxide sensors are short response/recovery time, small size and inexpensive fabrication cost[29] [30]. However, they have not been fabricated as a handheld e-nose yet due to high operating temperatures, which requires high power consumption for the operations[25]. In addition, metal oxide sensors are vulnerable to sulphuric compounds and ethanol, which makes their applications limited[31].

A **piezoelectric sensor** utilizes shifts in resonance frequency of sensing materials when gas molecules are adsorbed on a material surface[32]. A quartz crystal microbalance (QCM) is a good example of the piezoelectric sensor. AC voltage is applied across a piezoelectric quartz crystal, which actuates the device at its resonance frequency[31]. A thin layer membrane, which selectively adsorbs a target analyte, is coated on the quartz crystal, and when the gas molecules are adsorbed on the membrane, it increases the mass of the system and decreases the resonance frequency of the quartz crystal[27]. It has selectivity in the sense that different gas molecules have different adsorption coefficients on the sensing materials. Fast response times, less than 10 seconds, have been reported[33]. The disadvantages of a piezoelectric sensor are complex fabrication steps with interface circuitry and high noise signals in an ambient condition[34].

An **optical sensor** utilizes the change in optical properties of a fluorescent dye when in contact with vapor molecules. The dye is generally coated on the tips of optic fibers[34]. The optical properties of fluorescence mentioned here include the intensity, spectrum, lifetime and wavelength. The alteration of polarity in a fluorescent dye is the main factor causing these changes of optical properties[25]. The fluorescent-coated fiber tips are encapsulated in a polymer matrix to increase the stability. Thus, the sensitivity of this sensor depends on what type of fluorescent dyes or what type of encapsulating polymers are used[34]. Some metal oxide materials such as alumina are used as an adsorbent attached on the polymer to increase the sensitivity[35]. Optical sensors have few

advantages namely in its compact size and fast sensor response; less than 10s. However, the fabrication and operation costs are high due to the complexity associated with electronics and software. Moreover, they have a short lifetime because of the photochemical quenching of fluorescent dyes[34].

1.3 Challenges in developing electronic nose

In previous sections, we have reviewed the working principles, advantages and disadvantages of various types of chemical sensors introduced as e-nose. The advances in technology have enabled researchers to successfully enhance the sensitivity and improved the limit of detection, portability, energy efficiency and response time. Recently, many attempts have been made to address the challenges of poor chemical selectivity exhibited by many e-nose systems through pattern recognition algorithms in multi-array sensors with multi-chemoselective interfaces[36]. However, it is still difficult to find an optimal chemoselective interface, or receptor, which provides high selectivity to certain target molecules and prevents non-specific adsorption of background molecules. Interference is normally observed in the spectral response of a specific compound due to the presence of background molecules. The interaction between a sensor interface and background molecules disturbs a linear combination of target molecules. Therefore, the recognition of target molecules in multiple vapor mixtures has been a major challenge due to such background interferences.

The detection of volatile organic compounds (VOCs) is also a big challenge in developing an e-nose system. VOCs are organic chemicals which have high vapor pressures and comparatively low boiling points; less than or equal to 250 °C at standard atmospheric pressure of 101.3 kPa[37]. They include both artificially made and naturally occurring chemical compounds such

as acetone, ethanol, methane and formaldehyde. VOCs are commonly generated and used around us from many different sources such as paints, cars, smoke and animal refuses[38 39]. Industrial use of fossil fuels also produces numerous VOCs such as gasoline, benzene and naphtha. The detection of VOCs in a very low vapor concentration; parts-per-billion (ppb) level, has been successfully reported by many researchers using conductivity sensors. However, selectively detecting VOCs in a vapor mixture is still challenging because of the weak chemical or physical interaction between target components and sensor interfaces. This limits the retention time of target molecules and disturbs the fully selective detection with sensor arrays.

Some of the commonly generated VOCs around us are dangerous to animals and human beings, and harmful to the environment. Toluene affects the central nervous system and benzene causes a carcinogen and is an occupational hazard to human beings[40]. Exposed to the air containing 1 ppm of benzene for 8 hours per day can cause those problems. Perchloroethylene and methylene chloride are highly dangerous to human health; the former can cause cancers and the latter can cause symptoms similar to carbon monoxide exposure in human beings[41 42]. Mature tailing ponds generated by the oil sands industry in Alberta, Canada, consist of 1−3 wt % of residual bitumen and naphtha[43]. This small concentration of VOCs in tailing ponds can greatly damage the environment near the sites. In 2010, hundreds of migrating ducks died after landing on tailings water[44]. The biggest problem in detecting VOCs in industrial sites is that they appear at low concentrations and quickly disperse in the air. Shell Oil's Deer Park refinery released approximately 40,000 pounds of benzene in for 2 weeks in 2013, but no workers noticed the leakage at the site[40]. Thus, developing a novel e-nose system, which has a potential to sensitively and selectively detect VOCs in an ambient condition, is immediately needed.

1.4 Microcantilever sensor

Microcantilevers have been employed as a physical, chemical or biological sensor to detect molecules by deflections or resonance frequency shifts[45]. They have a wide range of applications especially in the field of environmental monitoring, air and water analysis, and in the field of medicine, detecting diseases and points of mutations[46]. Microcantilevers have shown a reproducible detection of target species with a wide concentration range from parts-per-thousand (ppth) to parts-per-trillion (ppt)[47–49]. In previous literature, it has been reported that they can detect ppt levels of organic vapor within seconds by analyzing the microcantilever deflection[50].

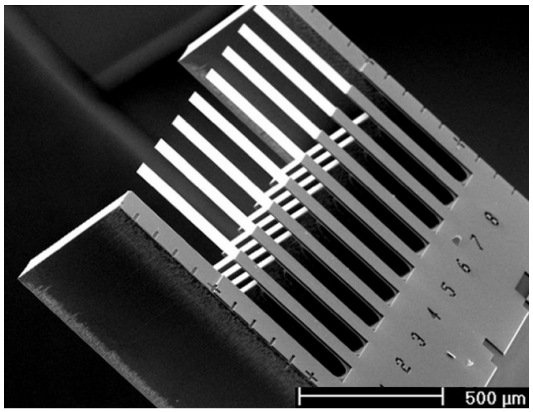

Figure 1.3. Scanning electron microscope (SEM) image of rectangular microcantilevers[51].

Figure 1.3 shows the SEM image of commercially used silicon (Si) microcantilevers. They have multi-element sensor arrays in one chip, which enables multiple patterning of the receptors to detect various target molecules. The microcantilever sensors provide several advantages over other conventional analytical techniques with their compact size, low power consumption, room-temperature operations and short recovery time[52–54].

Microcantilever sensors utilize the transduction of mechanical energy and mechanical phenomena when chemical and biomolecules are introduced onto the device interface. This is explained in two operational modes: dynamic mode and static mode. In dynamic mode, the resonance frequency of microcantilevers shifts following the molecular adsorption on a microcantilever surface[55–57]. By tracing the resonance frequency shift, the mass of adsorbed molecules on a microcantilever surface can be measured through the equation

$$f = \frac{1}{2\pi}\sqrt{\frac{k}{m^* + \alpha\Delta m}} \tag{1}$$

where the resonance frequency of a microcantilever, f, varies with the loading mass (Δm). k is the spring constant and m^* is the effective mass of a microcantilever and α is a numerical constant[57]. The detection of attogram scale (10^{-18} gram) mass changes of nanoparticles in an aqueous environment has been successfully demonstrated by using a microcantilever [58].

In static mode, a microcantilever bends with an applying stress on its surface[57]. The change in the Gibbs free energy on the surface induced by surface-analyte interactions and outer forces such as heat, electrical power and magnetic field make the microcantilever deflect[59]

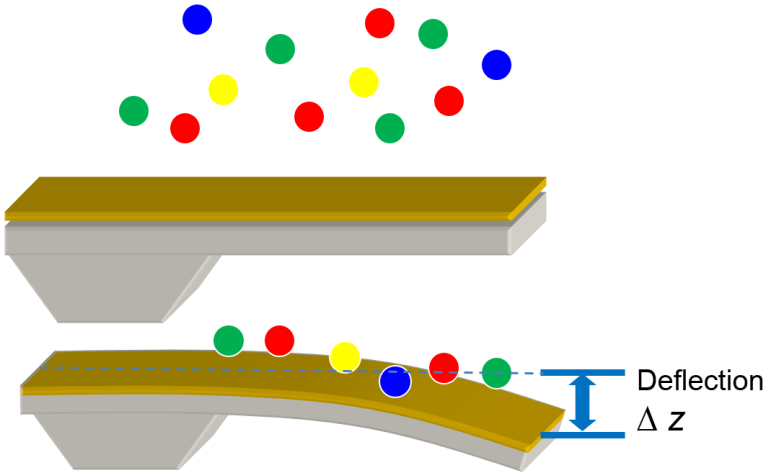

Figure 1.4. Static mode operation of the microcantilever sensor.

A microcantilever deflects once a sensing event occurs as shown in Figure 1.4. Adsorbed molecules generate a surface stress at the interface between the microcantilever surface and molecules, and this surface stress deflects the microcantilever[60]. The surface stress induced on the microcantilever can be measured according to the Stoney's formula[45]

$$\Delta\sigma = \frac{Et^2}{4R(1-\nu)} \tag{2}$$

where E is the modulus of elasticity, t is the thickness of the microcantilever, R is the bending radius of a microcantilever and ν is Poisson's ratio. The static mode of operation is efficiently used in order to detect target molecules even in a liquid phase. Thus, numerous biological applications such as selectively detecting DNA and cancer cells have been successfully performed by monitoring the deflection of microcantilevers[61].

There are mainly 4 ways to measure the deflection and resonance frequency of microcantilevers with high accuracy; optical reflection, capacitance measurement, piezoelectric

technique and piezoresistance technique[62]. **Optical reflection** method is the most commonly used method introduced in 1988[63]. A laser diode is focused at the tip of the microcantilever and reflected to a position sensitive detector (PSD) as shown in Figure 1.5.

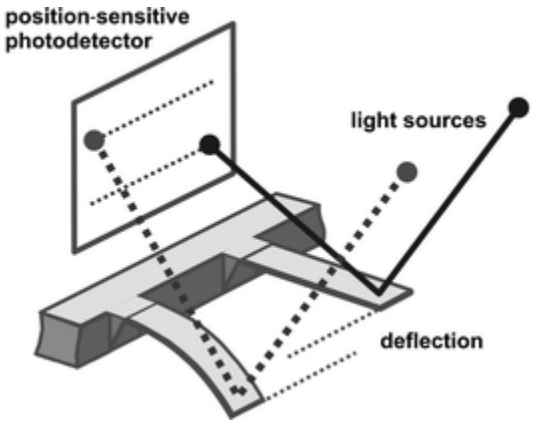

Figure 1.5. Microcantilever array readout scheme by optical reflection with PSD[64].

A PSD is an optical position sensor which measures the position of a reflected light spot in two-dimensions on the sensing surface. Exposing a PSD to a tiny spot of light creates a change in local resistance of the exposed area. This causes a shift in the electron flow in the electrodes of PSD and thus a location and intensity of the light spot are measured. The light spot shift of 0.1 nm can be measured precisely with PSD system. By tracing the shift of a light spot reflected from the microcantilever surface, we can measure the static deflection and resonance frequency of microcantilevers[65].

A fixed electrode on the microcantilever is required for the other three methods; capacitance, piezoelectric and piezoresistance techniques, in order to measure the deflection and

resonance frequency. In the **capacitance** measurement, the deflection of the microcantilevers can be estimated by measuring a capacitance variation between a conductor on the microcantilever surface and a fixed electrode[45]. The microcantilever deformation results in a change in the difference of these two capacitances. In the **piezoelectric** technique, a thin layer of piezoelectric material such as ZnO is coated on the microcantilever surface which generates an electric charge when the microcantilever bends[66]. This method is suitable for measuring the resonance frequency of microcantilevers. The **piezoresistance** technique utilizes a change in the electrical resistivity of a semiconducting or metallic microcantilever when a stress is applied on its surface[50]. The resistance change can be measured using a dc-biased Wheatstone bridge. This method is suitable for measuring the deflection of microcantilevers in static mode.

1.5 Microcantilever use in vapor detections

It has been demonstrated that microcantilevers provide an excellent sensing platform for the detection of gas phase analytes with high sensitivity. One of the first gas sensor applications with a microcantilever was reported by T.Thundat et al in 1995[67]. They detected a mercury vapor in the air with one side gold-coated silicon nitride microcantilevers.

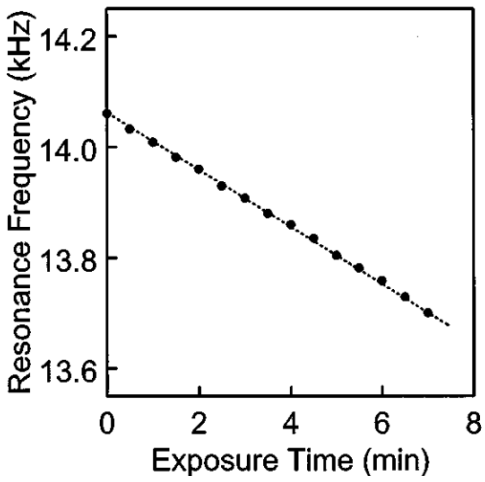

Figure 1.6. Resonance frequency shift of a silicon nitride microcantilever with one side partially coated with gold upon mercury vapor adsorption on the microcantilever surface[67].

When a gold layer was partially coated on the silicon nitride microcantilever surface, the resonance frequency was decreased when mercury vapors are introduced, due to the mass loading of mercury molecules on the gold coating area (Figure 1.6). The sensitivity of the bilayer microcantilever to the mercury adsorption was calculated ~0.7 pg/Hz in dynamic mode[67]. In contrast, the resonance frequency of the silicon nitride microcantilever was increased following the mercury adsorption when one side of the microcantilever was fully covered with gold[67]. This difference was explained as an increase in spring constant of the microcantilever from the mercury-gold amalgamation. When one side of silicon nitride was fully covered with gold, the increase in spring constant is more dominant than the resonance frequency decrease due to the mass loading of mercury, and it eventually resulted in increasing the resonance frequency of the microcantilever[67].

Numerous organic vapors were successfully detected by microcantilever sensors in the static mode and dynamic mode. Mercaptoethanol-induced microcantilever deflection of 0.432 nm

per ppb in a concentration range of 0-400 ppb was successfully measured using microcantilever deflection at 50 ppb levels has been reported by P. Datskos et al[68]. To enhance the selectivity of a microcantilever gas sensor, many people have coated various polymers on the microcantilever surface. A. Loui et al reported that they could selectively detect 10 different volatile organic compounds (VOCs) by coating 7 different polymers including poly (vinyl alcohol) and poly (4-vinylphenol) on multi arrays of a piezoresistive microcantilever[47]. Depending on the polymers coated on multi-arrays of the microcantilever, the deflection response curves of the microcantilever to VOCs were different. It is because each organic molecule has different affinity and diffusion rates to polymers. Also, various alcohols in a vapor phase could be differentiated based on their different molecular weight and molecular structure by tracing the response of PMMA coated microcantilever to the alcohol molecules[69].

A Self-assembled monolayer (SAM) of alkylthiolates and alkylsilanes on a microcantilever surface has shown a great enhancement of sensitivity in detecting organic gas molecules. A dramatic improvement of the response to 2,7-dimethylnaphtalene and tetrachloroethylene have been reported by modifying a nanostructured gold surface on microcantilevers with thiol receptors; having a limit of detection (LOD) as lows as 0.17 ppb and 0.28 ppm, respectively[69]. In addition, coating a hydrophobic hexamethyldisilazane with a sol-gel on a microcantilever surface showed a promising result for detection of a nonpolar organic vapor; it increased the microcantilever response to *n*-pentane vapor about 8 times[69].

Microcantilevers are also used as highly sensitive humidity sensors. The resonance frequency of a microcantilever changes due to the adsorption of water molecules on its surface. Ferrari et al coated hydrophilic poly(N-vinylpyrrolidinone) and poly(ethyleneglycol) on a microcantilever surface to enhance the affinity of water molecules on the microcantilever surface,

and obtained a resonance frequency shift of 1.5 Hz per relative humidity (RH, %) in a fundamental mode[70]. Later, a much higher sensitivity of 55 Hz shift per RH % and pico (10^{-15}) gram resolution of the water molecular adsorption were reported by T.Thundat et al by using a gelatine coated silicon nitride microcantilever[71]. A piezoresistive microcantilever coated with a 10 μm of humidity sensitive photoresist, which is capable of swelling by adsorption of water molecules on its surface showed a linear response of the resonance frequency shift to RH from 2 to 60 %[72].

1.6 Photothermal Cantilever Deflection Spectroscopy (PCDS): selectivity enhancement

Microcantilever sensors have shown an excellent selectivity by coupling their response with infrared (IR) spectroscopy. This combination of highly sensitive microcantilevers and highly selective infrared (IR) spectroscopy is called photothermal cantilever deflection spectroscopy (PCDS)[73]. It has generated a great synergy in chemical and biological sensing applications. The spectrum in the mid IR range is known as a molecular fingerprint regime because of the uniqueness of molecular vibrations in the region[49 74 75]. The adsorbed molecules on microcantilevers generate heat as the atomic vibrations of molecules are excited by IR[49]. This heat generated from adsorbed molecules deflects microcantilevers in static mode. Tracing the microcantilever deflection under IR, we can identify the adsorbed molecules on the microcantilever surface[76]. People have normally used bilayer microcantilevers for PCDS experiments. Two different materials have different thermal expansion coefficients and Young's modulus. When they are heated by adsorbed molecules under IR, one material expands faster than the other. Due to this difference in their heat expansions, bilayer microcantilevers bend toward the material which expands less[74 76 77].

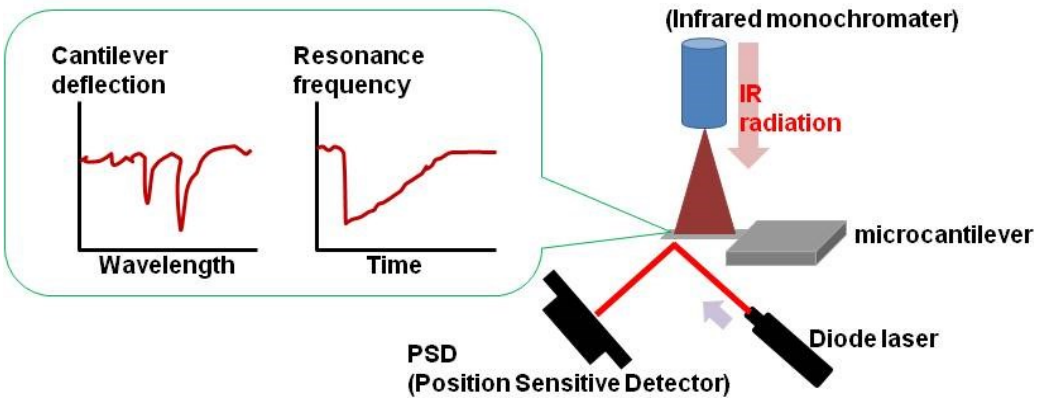

Figure 1.7. Schematic of PCDS sensor system using optical reflection[78].

Figure 1.7 shows the simple schematic of PCDS system including a microcantilever, IR source, diode laser and PSD. A diode laser is incident on the microcantilever surface and reflected to the PSD. The PSD signal provides the signal deflection and resonance frequency of the microcantilever.

PCDS uses the thermal response of microcantilevers under IR light. The thermal response of the microcantilever, which causes the microcantilever to deflect, is modified by the IR power, frequency and wavelength. The higher the power of IR, the greater the microcantilever deflection due to higher molecular absorption of the impinging IR photons. As the molecules absorb the IR, they transfer their heat to the microcantilever increasing the bending. S. Kim et al has reported that the deflection of the microcantilever linearly increases with the IR power [78]. The frequency of the microcantilever deflection is also decided by the pulse frequency of the IR. The microcantilever deflection is saturated after some time when it receives the constant amount of IR. Due to this fact,

pulsed IR at a specific frequency is normally used in PCDS to give enough time to microcantilevers to reach the saturated deflection points and come back to the original room temperature position.

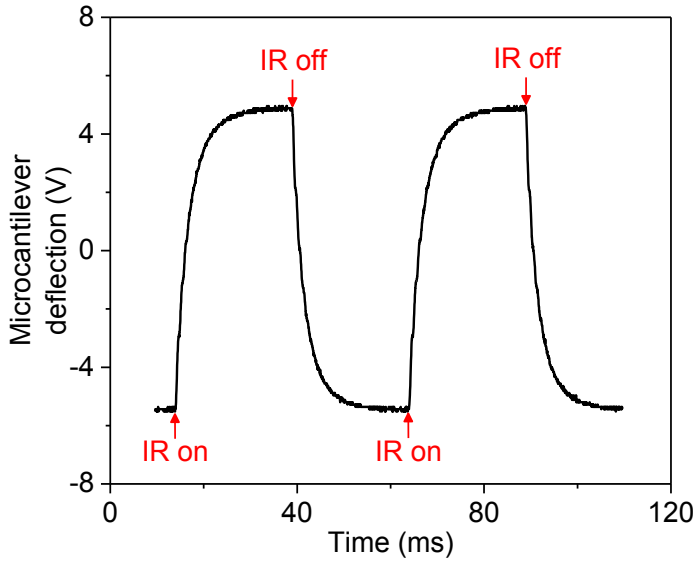

Figure 1.8. Thermal response of a microcantilever by shining pulsed IR at 20 Hz.

Figure 1.8 shows the deflection of a microcantilever under pulsed IR of 20 Hz. A gradual increase in the microcantilever deflection is observed the instant IR light is shone on the microcantilever surface. After 16 ms, the deflection of the microcantilever is saturated and the microcantilever stays at the same position. When the IR is off, the microcantilever deflection comes back to the initial position. By scanning the wavelength of IR with time, we can get an IR spectroscopy based on the microcantilever deflection.

The ternary vapor mixture of highly energetic organic materials (TNT, RDX and PETN) were successfully detected by using a receptor-free bilayer microcantilever with mid IR[78]. It was observed that pico-gram level of molecules on the microcantilever surface generated enough heat

to deflect the microcantilever. It showed the distinct response to the organic compounds[78]. A high limit of recognition (LOR) level on the microcantilever was reported with this method; TNT to PETN is 23 : 1, PETN to TNT is 32 : 1 and RDX to PETN is 30 : 1[78]. This ability of the PCDS technique to detect individual component from mixtures adds the real selectivity to microcantilever sensors. The PCDS also has strong advantages over other techniques from a commercial point of view. They have a real time *in situ* detection of target molecules in ambient conditions and a rapid response; it only takes few seconds to scan wide mid IR regions[36 79]. Therefore, PCDS can potentially approach the employment of an e-nose in diverse industrial and environmental monitoring with its high sensitivity, selectivity and applicability.

1.7 Nanoporous anodic aluminum oxide (AAO) microcantilevers: sensitivity enhancement

Numerous modifications of a sensor surface such as growing nanorods, fabricating nanowires and coating nanotubes have been implemented in order to increase the sensitivity with high surface area[80–82]. Over these types of modifications, an anodic aluminum oxide (AAO) nanowell structure has strong advantages in sensing applications.

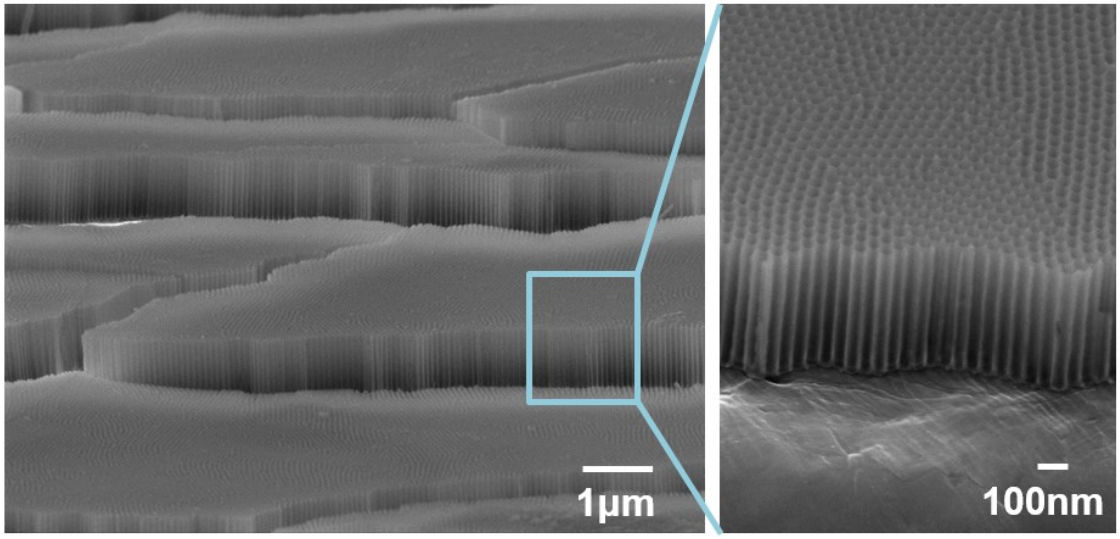

Figure 1.9. SEM images of nanoporous AAO film.

They have higher reproducibility and linearity than other nanostructures due to their precise control of nanowell dimensions[83]. Figure 1.9 shows very well-ordered and uniform AAO nanowells. The diameter, depth and interpore distance can be easily controlled from the self-ordering anodization process[84] [85]. This self-ordering anodization is a very cost effective, simple, fast and highly repeatable process as compared to other fabrication methods of nanostructures[86]. Also, aluminum oxide is a very attractive material to be used for gas sensing devices because it has a stability at a high temperature, and has a strong chemical resistance and affinity to adsorbed gas molecules[86]. It can work as a great platform for vapor analyte detections[87].

Vertically well-ordered AAO nanowells are formed through a two-step electrochemical anodization. Anodization is a process of naturally growing oxide layers on the surface of metals.

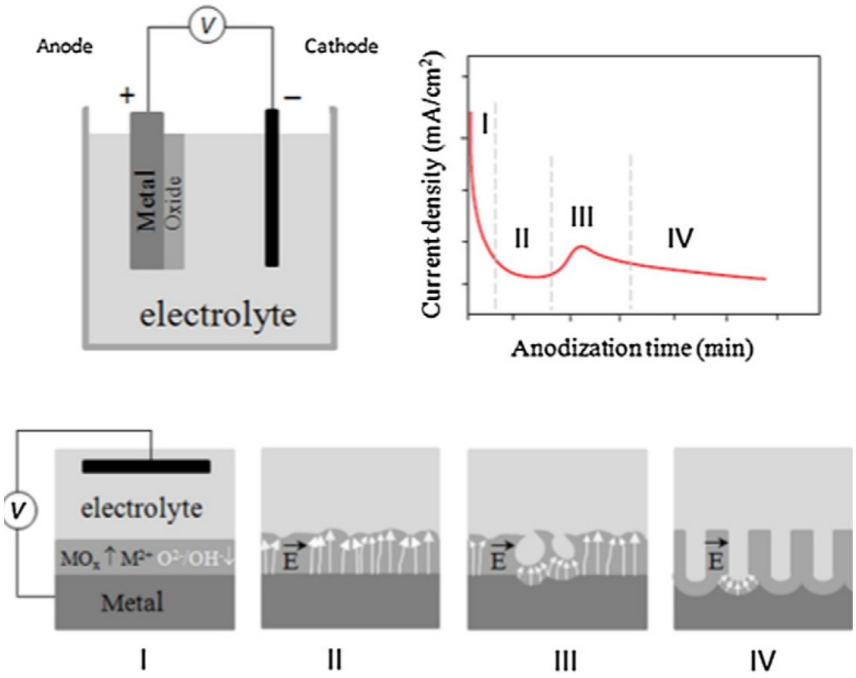

Figure 1.10. Schematic diagram of electrochemical set up for the vertically aligned AAO nanowell fabrication through the two-step self-ordering anodization and typical current density change with the anodization time. Stages of pore growth: formation of oxide layer from aluminum substrate (I), formation of pits by local electric field heterogeneities (II), initial random pores formation (III) and well-ordered pore growth (IV)[88].

Figure 1.10 shows the experimental set up for the AAO anodization, the current density change over time and the well-arranged nanowell aluminum oxide formation through the self-ordering anodization process. The anodized aluminum is grown on an aluminum substrate (anode) by passing direct current through an acid solution (electrolyte). This current releases hydrogen at a negative electrode (cathode) and oxide at the surface of aluminum anode[89]. Once the anodization starts, the aluminum surface is uniformly covered with an oxide layer and then the current drops over time as shown in the stage I in the graph. The electric current is localized on the aluminum

surface according to the surface roughness and the heterogeneity of the substrate. This causes the further suppression of current density on the oxide layer as shown in state II. The localized electric field assists the dissolution of the oxide layer in the acid solution, and this is when the pore formation occurs. The current fluctuates during this initial pore formation step as shown in state III. The electrical field is continuously concentrated on the pore pits and decreases along the pore walls. The continuous process of the formation and dissolution of the aluminum oxide layer above the pore pits assisted by the localized electric field forms periodic aluminum oxide nanowells[90]. The current is stabilized during the vertical aluminum oxide nanowell growths as shown in stage IV. After the 1st anodizing process, aluminum oxide nanowells are randomly distributed because of the current fluctuation at the initial stage. They are removed by aluminum oxide etchant solutions such as chromic acid; however, uniformly distributed pore pits still remain on the aluminum substrate. Through the 2nd anodization step, well-ordered aluminum oxide nanowells are grown on the aluminum substrate.

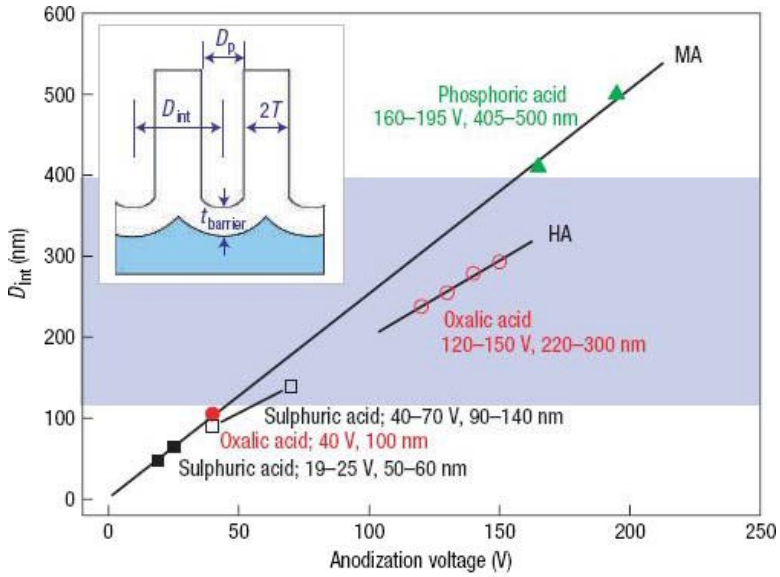

Figure 1.11. Regime of self-ordering anodization for the fabrication of nanoporous AAO[91].

The dimensions of AAO nanowells are dominantly influenced by anodization time, applied voltage and electrolyte type[88]. The effects of anodization voltage and electrolyte type on the interpore distance of the AAO nanopores are shown in Figure 1.11[91]. A wide range of AAO interpore distance (D_{int}) from 50−500 nm have been reported by using sulphuric acid, oxalic acid and phosphoric acid. In a certain electrolyte, a higher voltage makes a longer D_{int} of AAO. The pore diameter (D_p) is initially decided during the anodization process, and can be further increased by a simple pore widening process, dipping in a phosphoric acid solution. Approximately 20−450 nm of D_p has been reported so far[91]. Also, the thickness of nanowells is easily controlled by changing the anodization time. For example, anodization for 10 minutes and 20 minutes in the oxalic acid solution, 1 μm and 2 μm thick AAO nanowells are formed, respectively. A wide range of thickness from tens of nanometer to hundreds of micrometer have been reported[92]. This simple and exact control of nanowell dimensions is the main advantage of AAO nanopores over other nanostructures.

A novel fabrication method of nanoporous AAO microcantilevers by patterning microcantilever structure on AAO layer by photolithography was introduced by *P. Lee* et al in 2008[93].

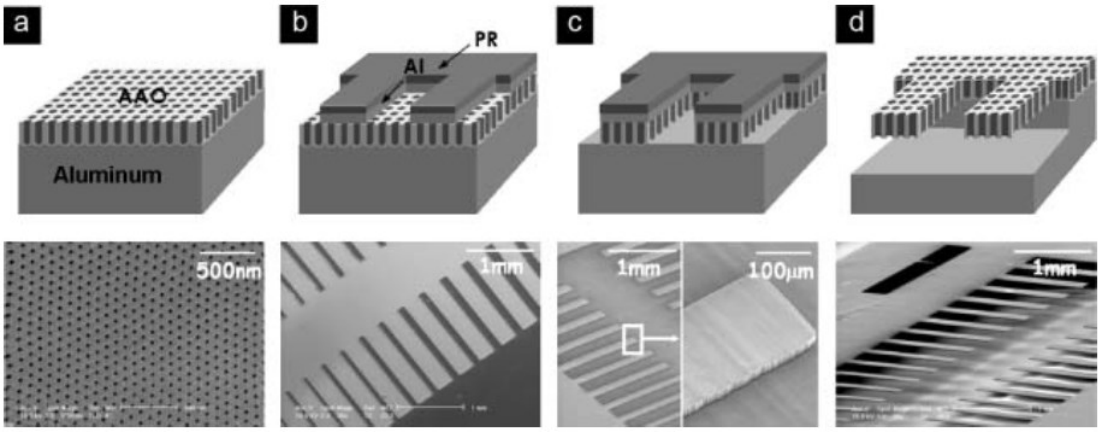

Figure 1.12. Patterning nanoporous AAO microcantilevers through photolithography. Well-ordered AAO layer is grown on aluminum substrate through two-step anodization (a). A microcantilever shape is patterned on top of the AAO layer after thin layer of aluminum and photoresist are deposited. AAO out of the pattern is etched (c), and the photoresist and aluminum layer on top and bottom sides are removed (d)[93].

Figure 1.12 shows the overall process of AAO microcantilevers fabrication by using photolithography after AAO is deposited on aluminum substrates through the two-step anodization. A few micrometers of AAO was deposited on the aluminum substrate, and then 500 nm of aluminum was coated on top. Microcantilever structures were patterned using a UV-photomask after a thin layer of photoresist was spin coated on the 500 nm aluminum layer. Microcantilever patterns of the aluminum and alumina layers were removed by dipping them in a mixture solution of phosphoric, nitric and acetic acids, and a phosphoric acid, respectively. The photoresist and aluminum layers on top of the AAO microcantilever patterns are also etched, and then the remaining aluminum substrate under AAO microcantilevers was lastly removed by electrochemical etching with a perchloric acid and ethanol solution.

Nanoporous AAO microcantilevers have shown much higher sensitivity in detection of gas phase molecules than other plain microcantilevers. The high surface area of nanopores provide large adsorption sites for target molecules. It leads to bigger resonance frequency shifts of AAO microcantilevers as more molecules are adsorbed. Porous structures have smaller Young's modulus than non-porous plains structures. Thus, AAO nanoporous microcantilevers deflect more than other non-porous stiff microcantilevers when molecules are adsorbed on the microcantilever surface.

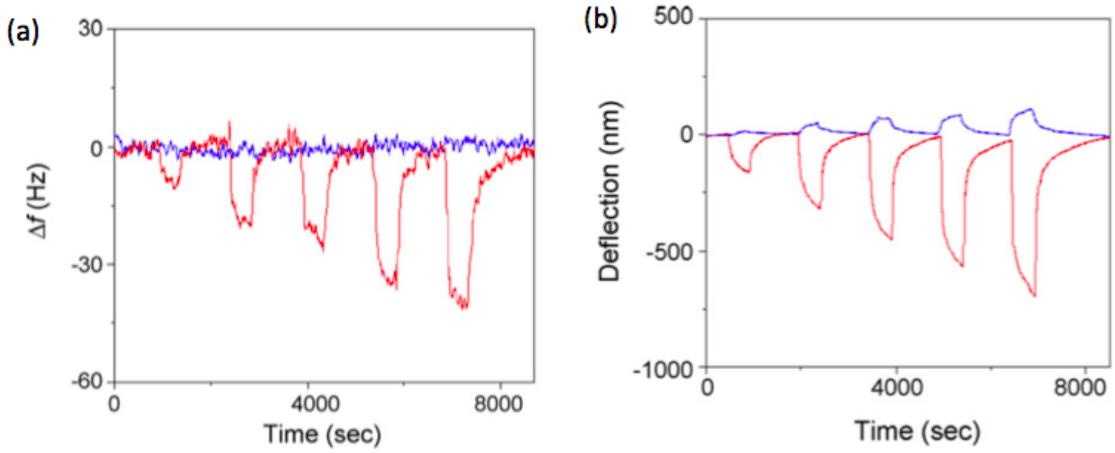

Figure. 1.13. Resonance frequency shift (a) and variation of deflection (b) of a plain Si microcantilever (blue) and AAO microcantilever with 50 nm pore diameter (red) during the adsorption and desorption of water vapors.

Figure 1.13 shows the difference in resonance frequency shift and deflection of a nanoporous AAO microcantilever and plain Si microcantilever when water vapor molecules are adsorbed on their surface. The plain microcantilever does not show any resonance frequency shift when 50−250 ppm water vapor is introduced; however, AAO microcantilever shows clear resonance frequency shifts in that concentration range. The magnitude of the AAO microcantilever deflection is also much higher than that of the plain Si microcantilever. The spring constant and Young's modulus of the nanoporous AAO microcantilever is found to be quite lower than that of the Si microcantilever. These low spring constant and Young's modulus of AAO microcantilevers also contribute to the higher deflection sensitivity toward humidity[83]. Not only water, but organic vapors such as dodechanthiol, trinitrotoluene and cyclotrimethylene trinitramine were tested with AAO microcantilevers, and they showed very high sensitivity to those organic molecules as well[93 94].

1.8 Summary of the project

In this project, we have proposed to develop a novel e-nose system for the detection of VOCs through the combination of highly sensitive nanoporous AAO microcantilevers and highly selective PCDS technique. Nanoporous AAO microcantilevers provide a large surface area for the adsorption of VOCs on the surface. The high aspect ratio of AAO nanopores may provide a greater retention time for VOCs allowing the vapor to remain inside the pores, increasing the IR spectral response. The high porosity and low Young's modulus of AAO microcantilevers are expected to increase the thermomechanical sensitivity in PCDS. The thermal response of AAO microcantilevers to IR is optimized by characterizing the mechanical property with the variation of nanopore diameters. We expect to recognize and quantify each organic component from vapor mixtures in humid condition by analyzing the PCDS spectrum and resonance frequency shifts. We have used a wide range of high power quantum cascade laser (QCL) to identify various patterns of atomic vibrations in organic molecules. The three commonly used VOCs are tested in this project; ethanol, acetone and petroleum ether. Ethanol is a type of alcohol, which has a C-O-H bonding, acetone is a simple ketone, having a C=O bonding, and petroleum ether is a mixture of alkanes, having multiple CH_2 and CH_3 bonds. At room temperature, the vapor pressure of ethanol, acetone and petroleum ether are very high; ~40 mmHg, ~180 mmHg and ~400 mmHg, respectively. These three VOCs are mixed in a vapor phase with controlled concentrations and introduced to the sensing chamber where AAO microcantilever is placed. Water vapor molecules are also added in this ternary VOCs mixtures to test if the system works properly in humid condition. The optical reflection method is used to measure the deflection and resonance frequency of AAO microcantilevers. We expect to successfully qualify and quantify each organic component from vapor mixtures by using PCDS based on nanoporous AAO microcantilevers.

Chapter 2. Fabrication & experiment

Outline: Fabrication of nanoporous AAO microcantilevers with different pore sizes through the self-ordering electrochemical anodization and photolithography are explained in this chapter. The design of mass flow controllers (MFCs), thermomechanical analysis set up and PCDS system are also described.

2.1 Materials and equipment for the AAO microcantilever fabrication

A high-purity aluminum sheet (99.99 %) was purchased from Alfa Aesar (Ward Hill, MA). Petroleum ether was obtained from Fisher Scientific (Pittsburgh, PA). Perchloric acid, oxalic acid, acetone, ethanol, chromium oxide, nitric acid, phosphoric acid, acetic acid and sulfuric acid were purchased from Sigma-Aldrich (St. Louis, MO) and were used as received. The photoresist (PR) HPR504 and 354 developer were purchased from VWR (Edmonton, AB) and were used in photolithography. In order to cool down and heat electrolytes during the two-step anodization and electrochemical polishing processes, we used refrigerated bath circulators from Fisher Scientific (Pittsburgh, PA). 308R multi coater for evaporation and sputtering system was purchased from Ted Pella (Redding, CA) and used in coating aluminum, chrome and gold on AAO substrates. The lithography process station including Solitec resist spinner and Solitec vacuum hot plate, and ABM mask aligner in the University of Alberta nanofab were used for the patterning of microcantilever structures on AAO substrates. Auger microprobe JAMP 9500F from JEOL (Peabody, MA) was used to take SEM images of AAO microcantilevers.

2.2 Self-ordering anodization

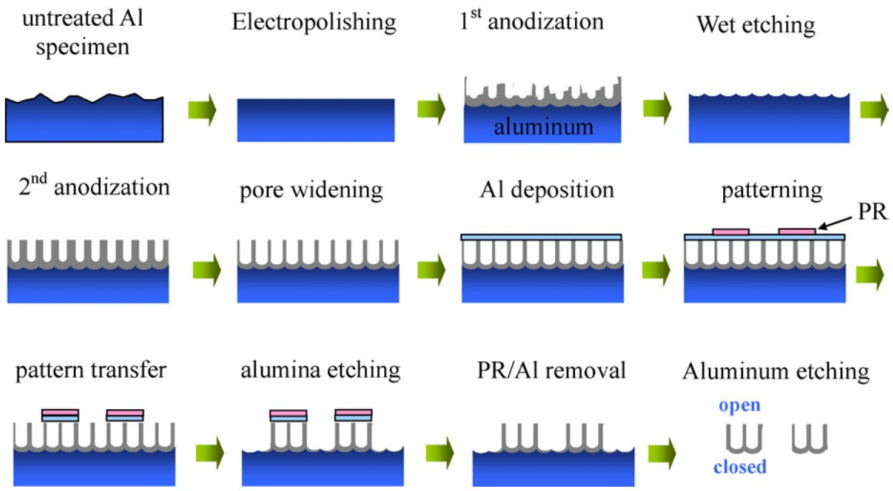

Figure 2.1. Procedure of the fabrication of AAO microcantilevers[83].

AAO microcantilevers are fabricated by the two-step anodization and photolithography as shown in Figure 2.1. Pure aluminum substrates are at first sonicated in acetone, and then rinsed with DI water to clean the surface. These substrates were electro-polished at 20 V for 5 minutes in a mixture solution of perchloric acid and ethanol (1:4 by vol %) at 5 $^{\circ}$C. Then, 1st anodization is performed in 0.3 M oxalic acid at 15 $^{\circ}$C for 10 hours, applying 40 V. After the 1st anodization, randomly shaped aluminum oxide nanopores are formed on the aluminum substrate. To remove these random nanopores, wet etching in a chromic acid and phosphoric acid mixture is performed. Hexagonally well-ordered 1μm thick nanoporous structures are made through the 2nd anodization, which is performed in the same sequence as the 1st anodization except for only 10 minutes. Higher thickness of AAO layers than 1 μm can be obtained through a longer anodization time. We performed the 2nd anodization for 15, 18 and 20 minutes, and obtained 1.5, 1.8 and 2.0 μm thick well-ordered AAO films, respectively.

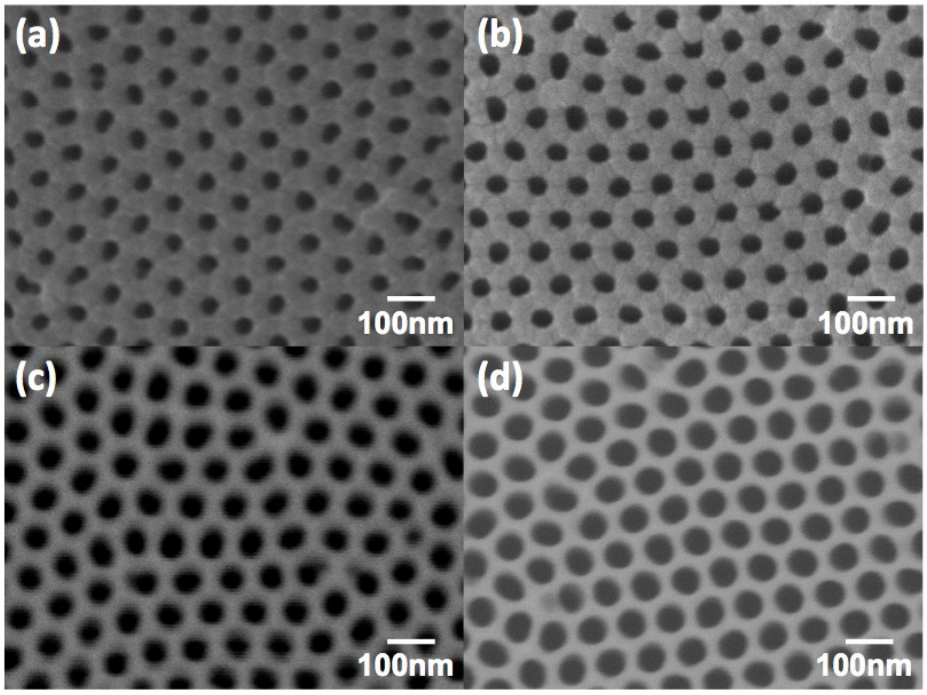

Figure 2.2. Top view of AAO nanopores with various diameters; (a) 35 nm, (b) 50 nm, (c) 60 nm and (d) 70 nm.

Figure 2.2 shows the SEM images of AAO nanopores with various pore diameters; 35, 50, 60 and 70 nm. The interpore distance of AAO is fixed at 100 nm when it is anodized at 40 V. The pore diameter is initially 35 nm, but bigger pores are made through the pore-widening process; dipping in 0.1 M phosphoric acid solution at 30 $^{\circ}$C. Dipping in the phosphoric acid solution for 20, 30 and 40 minutes, we obtained 50, 60 and 70 nm of pore diameters, respectively. Compared to the U-shaped nanopores made with other materials such as TiO_2 and Si, AAO nanopores are much more uniform and well-ordered. It's because AAO nanopores are formed from self-ordering anodization process. Each vertical nanowell is positioned like a hexagonal honeycomb.

We initially tried to make AAO with bigger pore diameters than 70 nm, but it was not possible at the anodization voltage of 40 V, because the interpore distance is fixed at 100 nm

applying 40 V. Nanopores were collapsed when we widened more than 70 nm. We found that bigger nanopores can be made through anodization at higher voltages from literature on AAO formations, and tried the 1st and 2nd anodizations at 50 V and 60 V[91].

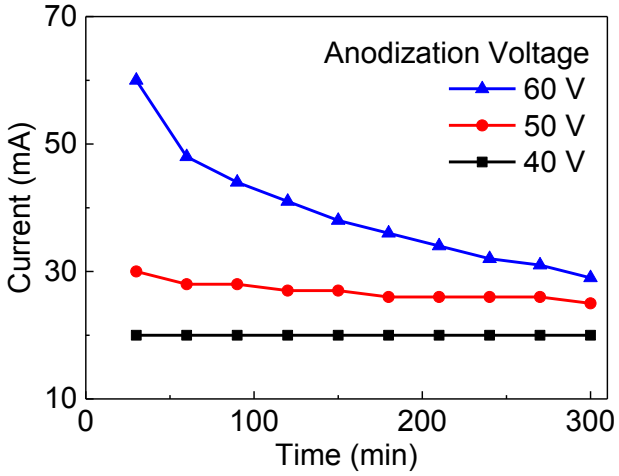

Figure 2.3. Current vs. time curves of constant applied 40, 50 and 60 V during the 1st anodization.

It is observed that the 1st anodization at 40 V proceeds at constant current of ~20 mA on aluminum exposed surface area of 4.5 cm^2. The current rapidly drops in several seconds at the beginning once the anodization is initiated. It is because of the formation of aluminum oxide layer on the aluminum substrate. It is stabilized after 1 or 2 minutes, forming well-ordered nanowells. It decreases approximately 10 % (from 30 mA to 27 mA) in 5 hours by applying 50 V, and it decreases around 50 % (from 60 mA to 30 mA) in 5 hours by applying 60 V with the same surface area of aluminum substrates. The 2nd anodization was performed with the same voltages.

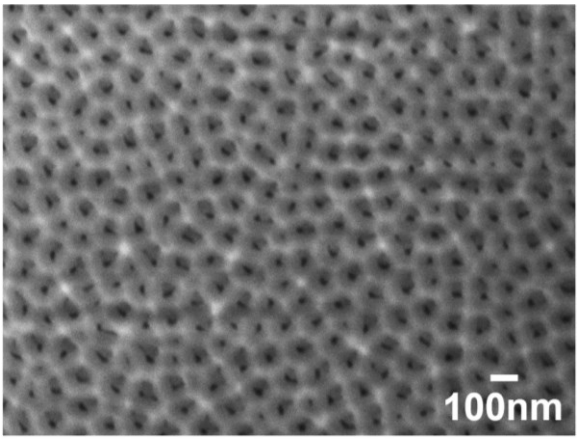

Figure 2.4. Randomly placed AAO nanopores from the two-step anodization at 60 V.

The AAO nanopores were randomly formed after the 2nd anodization at 60 V as shown in Figure 2.4. By getting this result, we could conclude that the electrical current on aluminum substrates during the anodization process should not be changed much after the rapid drop at the initial stage to form well-ordered AAO nanowells. In contrast to 60 V, well-ordered nanowells were formed when 50 V was applied.

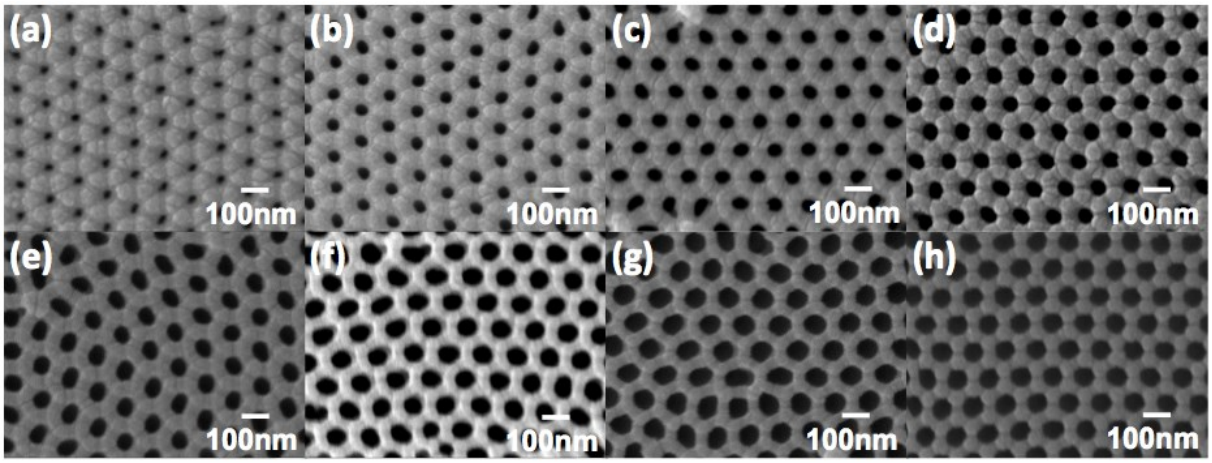

Figure 2.5. Top view of well-ordered AAO nanopores from the two-step anodization at 60 V. Various pore diameters; (a) 40 nm, (b) 55 nm, (c) 65 nm, (d) 73 nm. (c) 80 nm, (f) 86 nm, (g) 88 nm and (h) 90 nm were obtained through the pore widening process after anodization.

Various pore diameters with fixed interpore distance at 120 nm after the two-step anodization at 50 V are shown in Figure 2.5. When 50 V is applied, the interpore distance was increased by 20 % and the pore diameter was 5 nm bigger (40 nm) than the AAO nanopores anodized at 40 V as shown in the SEM images.

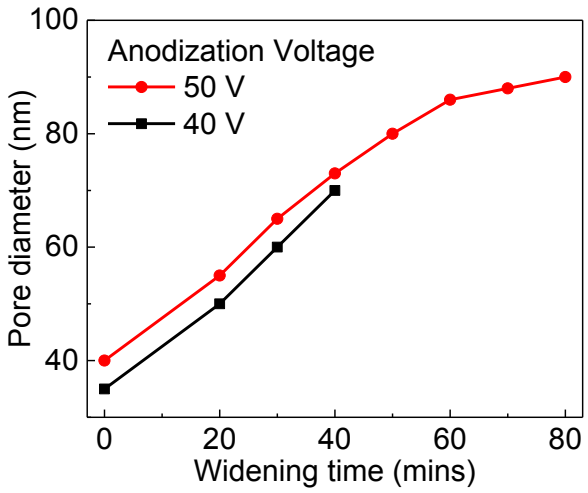

Figure 2.6. AAO nanopore diameter vs. widening time curves after two-step anodization at 40 V and 50 V, and pore widening.

Figure 2.6 shows the increase in nanopore diameters of AAO as a function of widening time after the two-step anodization at 40 V and 50 V. The longer time we dipped AAO in 0.1 M phosphoric acid solution, the bigger nanopores were obtained. Through the self-ordering anodization process using an oxalic acid and simple widening process using phosphoric acid, we could obtain various diameters of AAO, ranging from 35 to 90 nm.

2.3 Patterning AAO microcantilevers

In order to fabricate AAO microcantilevers for the VOCs detection, a patterning of microcantilever structures on AAO film through a photolithography and electrochemical aluminum etching was performed. At first, 500 nm thick aluminum was coated on the open side of AAO layers by using the thermal evaporator at 0.3 nm/s rate followed by spin coating a photo resist (PR) on top of it; spreading at 500 rpm for 10 seconds and spinning at 4,000 rpm for 30 seconds. It was heated at 115 °C for 90 seconds, and then microcantilever beam patterns were transferred by using UV mask onto the photoresist (PR) layer. UV light was shone for 3 seconds to pattern microcantilever shapes on AAO layers. UV light quickly breaks the cross-links of PR. The reacted PR under UV light was rinsed by dipping the patterned AAO substrates in 354 developer for 20 seconds. The PR-uncovered aluminum areas were removed with a mixed etching solution of phosphoric acid, nitric acid, acetic acid, and water. Also, the exposed AAO was etched by dipping the substrates in phosphoric acid solution for 1 hour. The rest of PR and 500 nm aluminum layers were removed by dipping in acetone and the same aluminum etching solution above. The last step was removing the aluminum substrates on the bottom side. We electro-polished the aluminum substrates at 20 V for 3 hours in a mixed solution of perchloric acid and ethanol (1:4 by vol %) at 5 °C. Translucent microcantilevers were seen after this process. They were washed with methanol, dried with N_2, and then stored in a vacuum chamber for future experiments.

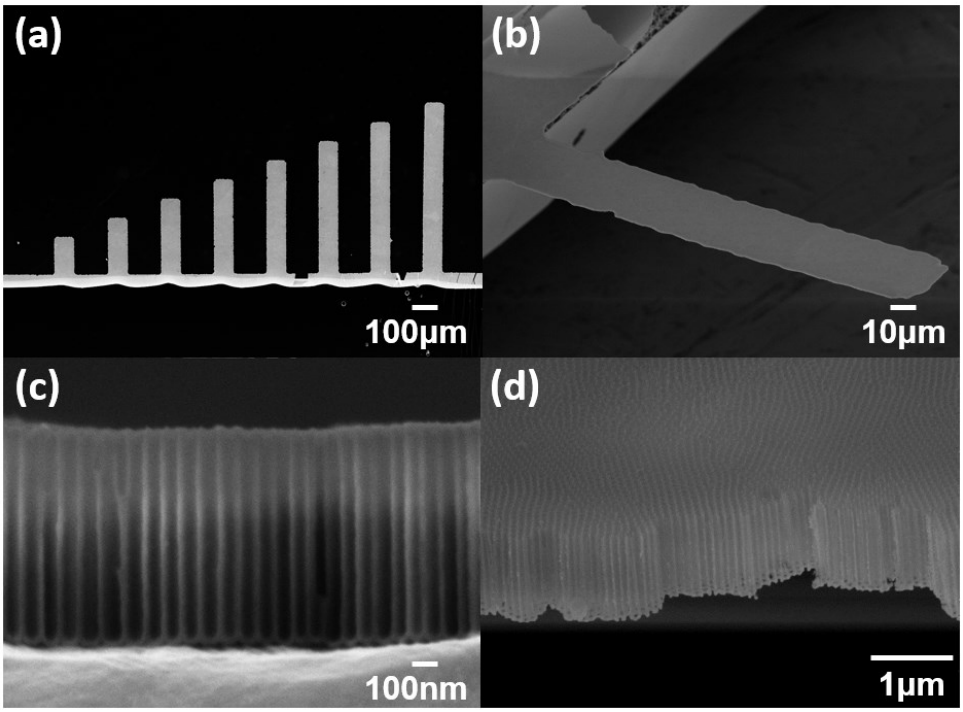

Figure 2.7. (a) SEM images of AAO microcantilevers with different lengths ranging from 180 to 810 μm and a width of 90 μm. (b) One AAO microcantilever beam is hanging. The side view of 1 μm thick AAO layer (c) before and (d) after removing the supporting aluminum substrate from the bottom.

Figure 2.7 shows the SEM images of 1 μm thick AAO layer and AAO microcantilevers at different magnifications. These microcantilevers were anodized at 40 V. Figure 2.7a shows 8 microcantilevers with different lengths ranging from 180 to 810 μm and a width of 90 μm. The thickness, interpore distance and pore diameter of AAO were 1 μm, 100 nm and 60 nm, respectively, confirmed by the side view image shown in Figure 2.7c. The top-side of AAO microcantilevers is open while the bottom side is closed. Figure 2.7b and d show that the AAO microcantilever beam is hanging in the air after the aluminum layer is removed from the bottom.

5 nm of Ti as an adhesion layer and 50 nm of gold were coated by using the thermal evaporator on the bottom side of AAO microcantilevers to make them bilayer for PCDS experiments.

2.4 Generation of VOCs vapor phase mixtures

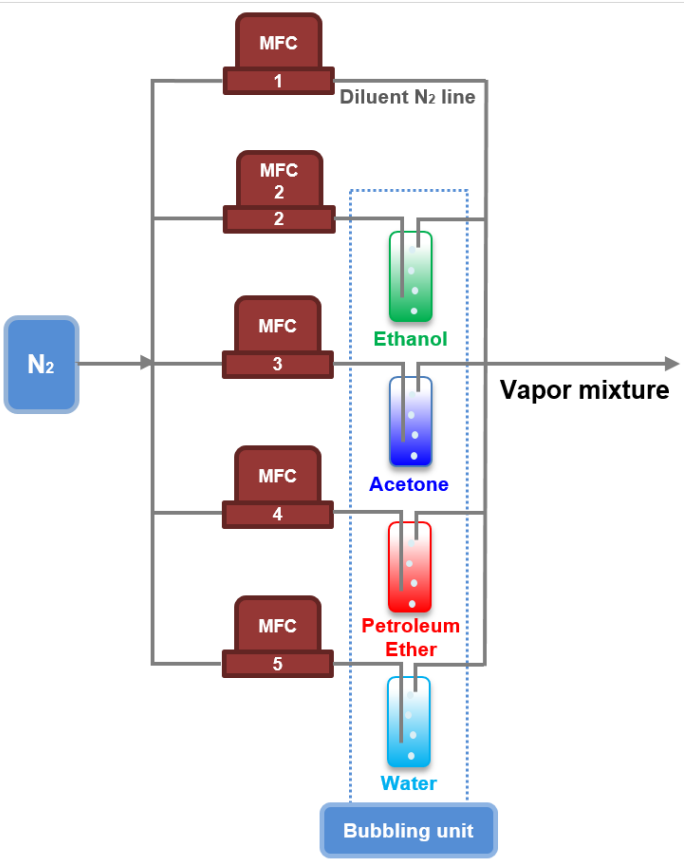

Figure 2.8. Schematic of generating VOCs in vapor phase.

Multiple mass flow controllers (MFCs) were used to control the vapor concentration of ethanol, acetone, petroleum and water as shown in Figure 2.8. A handmade bubbling unit was included to generate VOCs in vapor phase from liquid solutions. 5 channels of N_2 flow rate were controlled by digital MFCs from Atovac (Suwon, South Korea). One channel was used as a N_2 diluent gas flow and 4 channels were used to carry ethanol, acetone, petroleum ether and water

vapor molecules. Using this in-house built MFCs system, we could accurately control the flow rate of each N_2 flow line in a range of 0-100 standard cubic centimeters per minute (sccm), with a calibrated accuracy of 1 %. The concentration of each compound was calculated using a dilution equation[47]

$$\text{concentration} = \left(\frac{F_c}{F_c + F_d}\right)\left(\frac{P_s}{P_c}\right)\left(10^6\right) \tag{3}$$

where P_c is the carrier gas pressure, P_s is the solvent vapor pressure, and F_c and F_d are the carrier and diluent gas flows, respectively. Total vapor flow rate of 100 sccm was used in experiments.

2.5 PCDS experiment set up

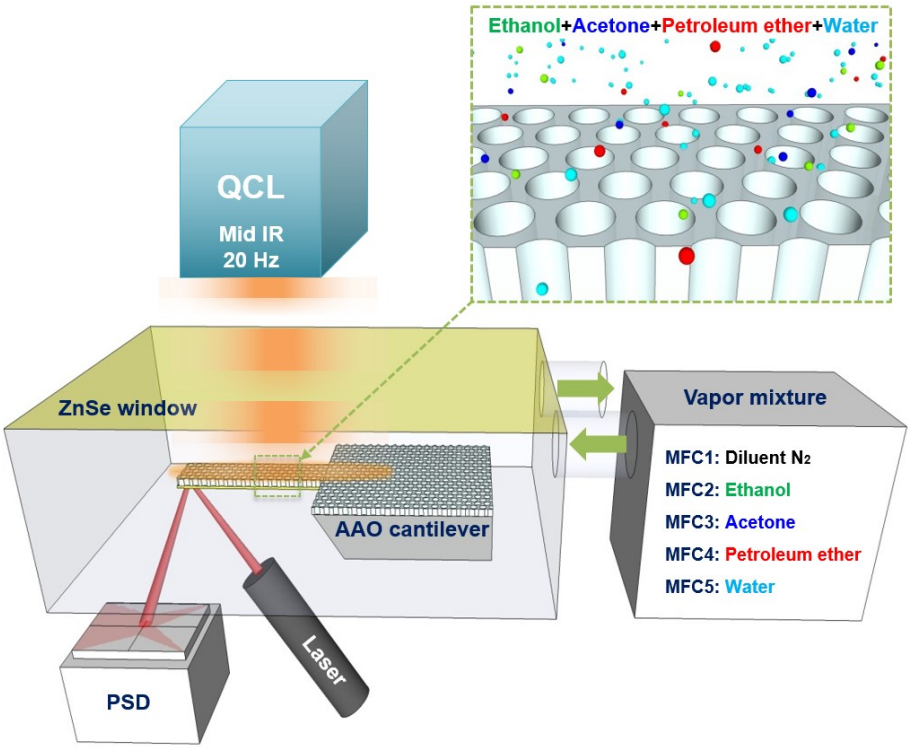

Figure 2.9. Schematic illustration of a gold-coated nanoporous AAO microcantilever and multi-channeled MFCs system for the detection of VOCs by using PCDS.

The schematic of the experimental setup used in this study is shown in Figure 2.9. A gold coated nanoporous AAO microcantilever is mounted inside a quartz flow cell, which is connected to the MFC's flow. The quartz flow cell is covered with a ZnSe window for IR transmission and placed inside the head unit of a multimode atomic force microscope (AFM) (Bruker, Santa Barbara, CA). Three different quantum cascade lasers (Daylight Solutions UT-6, UT-8 and MIRcat) were used as high power IR sources in a wide range of wavelength from 5.68 μm to 10.4 μm (1760 cm^{-1} to 961 cm^{-1}). A 200 kHz pulsed IR with 10 % duty cycle from the UT-8, and 100 kHz pulsed IR with 5 % duty cycle from the UT-6 and MIRcat were electrically modulated at 20 Hz by using a function generator DS345 (Stanford Research Systems, Sunnyvale, CA), and directed to the microcantilevers. This modulation of IR with function generator was applied because the microcantilever deflection is not as fast as the IR pulse frequency from QCL. The IR spectra were recorded using an SR850 lock-in amplifier (Stanford Research Systems, Sunnyvale, CA), and plotted with LabVIEW software (National Instruments, Austin, TX). The resonance frequency of nanoporous AAO microcantilevers was measured using an SR760 spectrum analyzer (Stanford Research Systems, Sunnyvale, CA).

2.6 Thermomechanical sensitivity analysis

Thermomechanical sensitivity of nanoporous AAO microcantilevers was measured by using a micro ceramic heater of which the temperature is regulated by a heater controller (GLTC-PX9 Global Lab, Seoul, Korea) and LabVIEW software. The temperature of this system was calibrated by using an indium microcantilever. We checked the indium microcantilever deflection slope changes at the melting-to-crystallization phase transition[95]. The temperature was cycled between 30 °C and 45 °C with a heating and cooling rate of 2 °C/min and 1.3 °C/min, respectively[78].

The voltage signal change (V) on the PSD was calibrated to the microcantilever deflection distance (μm) by using an MSA-500 micro system analyzer (Polytec, Irvine, CA).

Chapter 3. Results and discussion

Outline: This chapter contends the results and discussions of volatile organic compounds (VOCs) detection; ethanol, acetone and petroleum ether in vapor phase mixtures. We used photothermal cantilever deflection spectroscopy (PCDS) based on nanoporous anodic aluminum oxide (AAO) microcantilevers.

3.1 Adsorption of VOCs on AAO microcantilevers

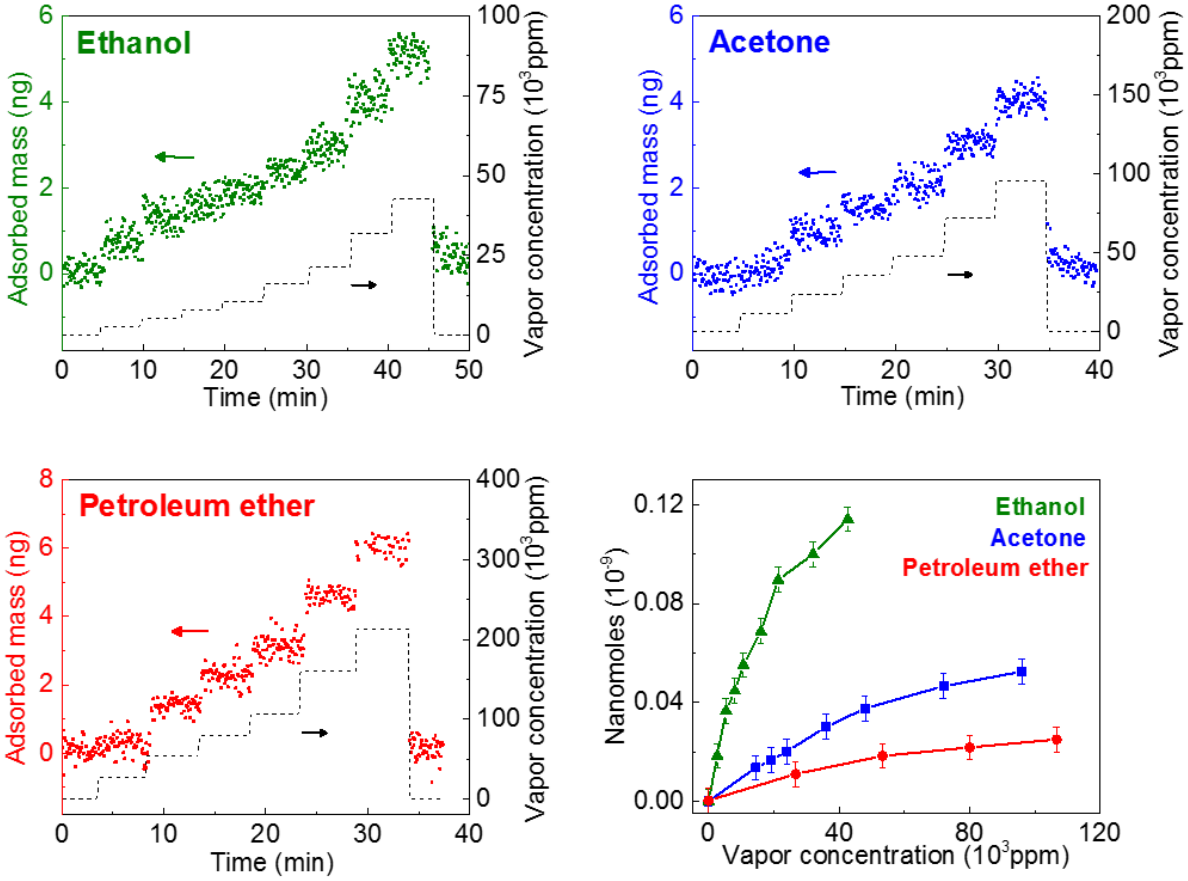

Figure 3.1. Adsorbed mass of three VOCs; (a) ethanol, (b) acetone and (c) petroleum ether on AAO microcantilevers (540×90×2 μm^3) with 70 nm pore diameter. (d) Adsorbed nanomoles of each VOC on AAO70 as a function of vapor concentration.

In general, a solid surface acts as a pre-concentrator for vapor molecules[87]. It is expected that the concentration of an analyte on the solid surface is orders of magnitudes higher than that in the air. This ability of solid surfaces is advantageous for most sensing systems in detecting vapor molecules. Figure 3.1 shows the adsorbed mass of three different VOCs on 70 nm pore diameter AAO microcantilever (AAO70) with a variation of vapor concentration. Initially, only N_2 vapor is introduced to the flow chamber where the AAO70 is. Through the MFC setup and bubbling unit, ethanol, acetone, and petroleum ether vapor molecules are individually added into the flow. The adsorbed mass of the VOCs on AAO70 was calculated by tracing the resonance frequency shifts. The 2nd oscillation mode was used to measure the adsorbed mass of VOCs as it is more sensitive to an additional mass than the 1st mode[96]. The relationship between adsorbed mass and higher resonance frequency shift is given by[70]

$$f_n = \frac{1}{2\pi}\sqrt{\frac{k_{n\ eff}}{m_{n\ eff}}} \tag{4}$$

where f_n is the resonance frequency, $k_{n\ eff}$ is the effective spring constant and $m_{n\ eff}$ is the effective mass of a microcantilever considered with the geometric factor. Assuming that the vapor molecules are uniformly adsorbed on the microcantilever surface, the adsorbed mass of the molecules were calculated with the approximated equation[97]

$$\frac{\Delta m_{eff}}{m_{eff}} \approx \frac{\Delta m_{actual}}{m_c} = -2\left(\frac{\Delta f_n}{f_n}\right) \tag{5}$$

where Δm_{actual} is the mass of adsorbed molecules, m_c is the actual mass of a microcantilever beam and Δf_n is the resonance frequency shift. By using this equation, the adsorbed mass of ethanol, acetone, and petroleum ether on AAO microcantilevers was calculated. The m_c of nanoporous AAO microcantilevers is calculated based on the density of aluminum oxide, 3.95 g/cm^3, and their porosity. The porosity (P) of AAO microcantilevers is related to the radius (r) of the nanopores and the interpore distance (d), and can be calculated by a simple equation.

$$P = \frac{\pi r^2 / 2}{\sqrt{3} d^2 / 4} = \frac{2\pi}{\sqrt{3}} \left(\frac{r}{d} \right)^2 \tag{6}$$

The interpore distance is fixed at 100 nm from the anodization at 40 V. The porosity of AAO70 was calculated to be 0.44 based on Eq 6. In all three cases; ethanol, acetone, and petroleum ether, the adsorbed mass on AAO70 increased with the vapor concentration. Adsorbed nanomoles of ethanol, acetone, and petroleum ether on the AAO microcantilever as a function of the vapor concentration is also plotted in order to compare their affinity to AAO nanopores as shown in Figure 3.1d. A much higher number of ethanol molecules are adsorbed on the same AAO microcantilever when compared to acetone and petroleum ether, which means that the affinity of ethanol molecules to the AAO surface is stronger than acetone and petroleum ether. This is probably because AAO is a hydrophilic material, and so the highly hydrophilic ethanol molecules are more strongly attached to its surface than the less hydrophilic acetone and petroleum ether molecules.

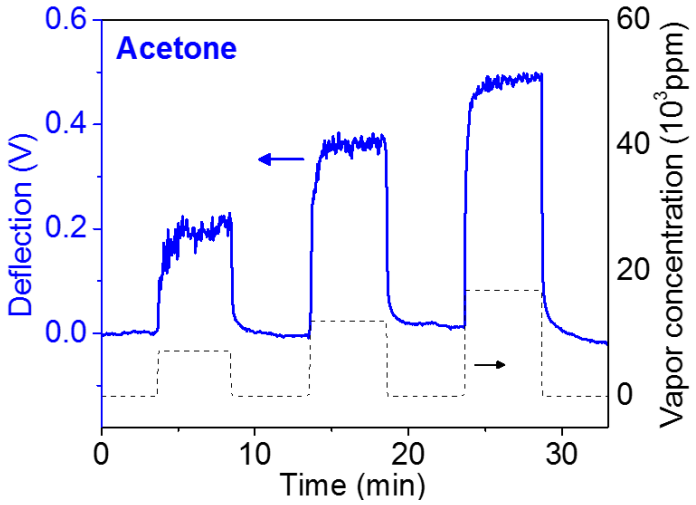

Figure 3.2. The variations in the deflection of AAO70 during the adsorption and desorption of acetone vapor molecules.

Figure 3.2 shows the variations in the deflection of AAO70 when it is exposed to the various concentration of acetone vapor. Dry N_2 was flowed for 10 minutes prior to introducing VOCs to remove moisture from the surface of AAO70. When the deflection became constant, which means that water molecules were evaporated from the surface, we started flowing acetone vapor and measured the deflection. AAO70 bent toward the open side. The adsorption of acetone molecules onto AAO70 induces compressive stress, making the microcantilever bend upward, possibly due to the acetone molecules adsorbed more on the open AAO nanopore side than the closed side. The adsorption and desorption of VOCs on AAO70 was very fast as shown in Figure 3.1b and Figure 3.2. Once the VOCs molecules are inserted and removed from the flow line, the resonance frequency and deflection of AAO70 immediately reached the steady state. In practical terms, this is an advantage of AAO microcantilevers to detect VOCs because they have a fast response and are self-regenerative.

3.2 Optimization of AAO microcantilevers for VOCs detection

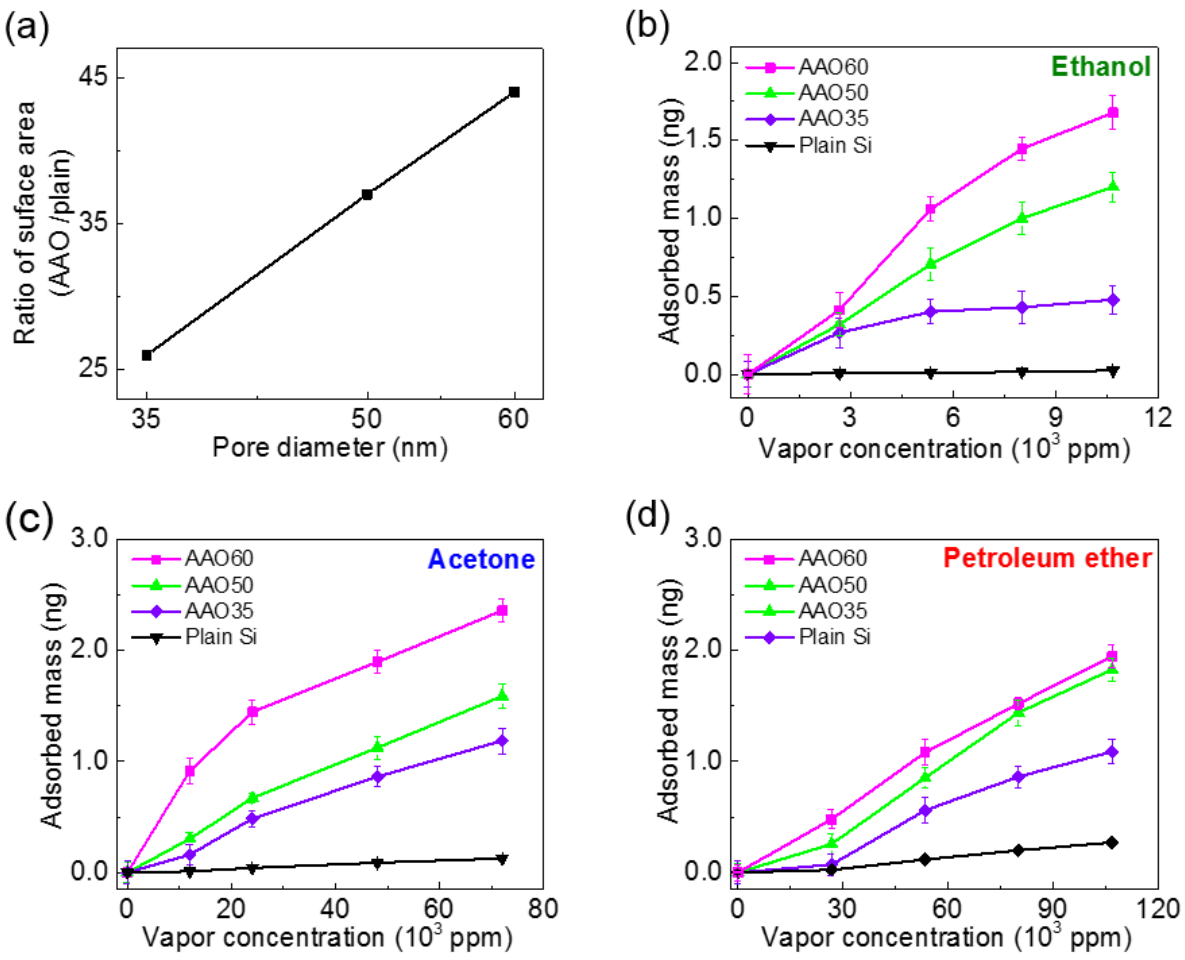

Figure 3.3. (a) Ratio of the surface area of AAO microcantilever/plain as a function of its pore diameter by a mathematical calculation. Adsorbed mass of (b) ethanol, (c) acetone, and (d) petroleum ether on AAO microcantilevers (540×90×1 μm^3) with different pore diameters; 35 nm (AAO35), 50 nm (AAO50) and 60 nm (AAO60), and a plain Si microcantilever (500×90×1 μm^3) as a function of vapor concentration.

Compared with U-shaped nanoporous films of other materials such as TiO_2 and Si, nanoporous AAO has a much more ordered and uniform structure. Also, it is very simple and easy

to control the pore diameters[98]. Thus, nanoporous AAO is an excellent platform to explore the influence of a pore diameter and porosity on a sensing performance. By the van der Waals interaction between the VOCs and the microcantilevers, vapor molecules are physisorbed on the surface. Figure 3.3a shows that the ratio of surface area, AAO to plain, increases linearly with the pore diameter. The interpore distances of AAO is fixed at 100 nm as it is anodized at 40 V. The surface area of AAO microcantilevers are 26 (AAO35), 37 (AAO50) and 44 (AAO60) times higher than that of the plain microcantilever with an identical unit volume. This higher surface area of AAO nanopores leads to the enhancement of sensitivity in detecting VOCs as it offers more adsorption sites where vapor molecules are adsorbed. Figure 3.3b and d shows the mass loading of ethanol, acetone, and petroleum ether on AAO35, AAO50 and AAO70 at various vapor concentrations. A plain Si microcantilever, which had similar dimensions was also tested for the comparison between nanoporous structures and a plain microcantilever. The dimensions of AAO microcantilevers are 540 μm in length, 90 μm in width and 1 μm thick. The plain Si microcantilever had a similar size; length of 500 μm, width of 90 μm and thickness of 1 μm. Adsorbed mass of organic vapor molecules on both nanoporous AAO microcantilevers and the plain Si microcantilever increased as a function of vapor concentration. In the case of ethanol, ~10, ~32 and ~46 times greater mass loadings on AAO35, AAO50 and AAO60 than the plain Si microcantilever were observed. It also shows the same trend that more molecules are adsorbed on bigger pore diameters of AAO microcantilevers in the case of acetone and petroleum ether.

The pore diameter of AAO, which is directly related to the porosity of the material, is expected to affect its thermo-mechanical sensitivity of bilayer microcantilevers as its Young's modulus, thermal expansion coefficient and thermal conductivity vary with their porosity. The decreased Young's modulus and hardness, caused by increasing the porosity of AAO, were

expected to contribute to the thermo-mechanical sensitivity of a gold-coated bilayer AAO microcantilevers based on theoretical calculations. Thermo-mechanical sensitivity of bilayer AAO microcantilevers with different pore sizes were calculated by using the bilayer microcantilever deflection equation[79]

$$z = -\frac{3}{4}(\alpha_1 - \alpha_2)\frac{t_1 + t_2}{t_2^2 K}\frac{l^3}{(\lambda_1 t_1 + \lambda_2 t_2)w}P \tag{7}$$

$$K = 4 + 6\left(\frac{t_1}{t_2}\right) + 4\left(\frac{t_1}{t_2}\right)^2 + \frac{E_1}{E_2}\left(\frac{t_1}{t_2}\right)^3 + \frac{E_2}{E_1}\left(\frac{t_2}{t_1}\right) \tag{8}$$

where z is the deflection of the bilayer microcantilever, α is the thermal expansion coefficient, λ is the thermal conductivity and P is the power which the microcantilever receives. The dimensions l, t and w are the length, thickness and width of the microcantilever, respectively. The subscripts 1 and 2 mean original material of the microcantilever and coated material. For gold-coated AAO microcantilevers, which were used in our experiments, the original material is AAO and the coated material is gold. The parameter K stands for the expression with Young's modulus (E) and thickness of the microcantilever.

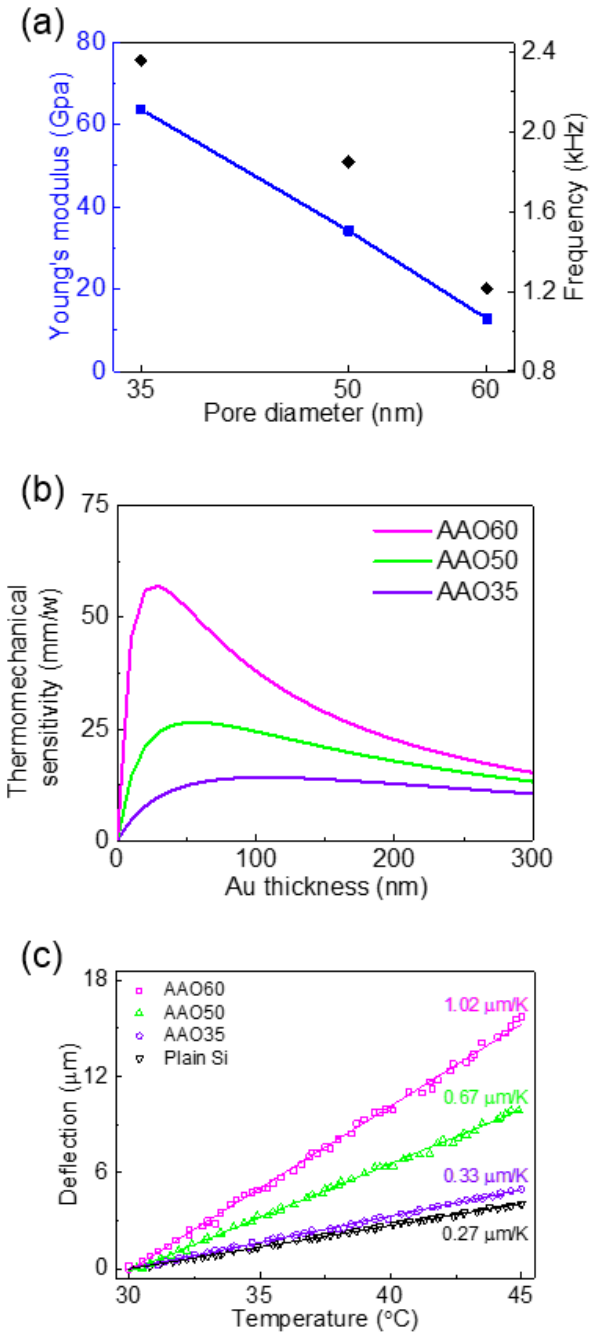

Figure 3.4. (a) Resonance frequency (black) and Young's moduli (blue) of nanoporous AAO microcantilevers with various pore diameters. (b) Theoretical calculation of the thermomechanical sensitivity of the gold-coated 1 μm thick AAO microcantilever with 35 nm (AAO35), 50 nm (AAO50) and 60 nm (AAO60) pore diameters as a function of a gold thickness. (c)

Thermomechanical sensitivity measurement of a 50 nm gold-coated AAO35 (purple), AAO50 (green) AAO60 (pink) and the plain Si microcantilever (black).

The Young's moduli of AAO35, AAO50 and AAO60 were obtained by measuring the 1st mode resonance frequency as shown in Figure 3.4a. The Young's moduli of AAO microcantilevers are linearly decreased as the pore diameters increased from 35 to 60 nm, which means that the AAO microcantilevers become physically more flexible with the increase in their porosities. Using the Young's moduli data obtained, thermomechanical sensitivities of AAO microcantilevers ($540\times90\times1$ μm^3) as a function of gold thickness were calculated and plotted (Figure 3.4b) based on the equation 7 and 8. The thermomechanical sensitivities rapidly increase with the gold thickness in the range of 30 ~ 100 nm depending on the pore diameters and then, they decrease. Also, the thermomechanical sensitivity of AAO bilayer microcantilever is enhanced by increasing the pore diameter from our calculation. This is due to the fact that the gap between the Young's modulus and thermal expansion coefficient of AAO and gold increases with the porosity of AAO. Experimental results (Figure 3.4c) confirm this theoretical approach as the 50 nm gold coated AAO60 showed higher thermomechanical sensitivity, 1.021 μm/K, than other AAO microcantilevers with smaller pore diameters; 1.5 and 3.2 times higher than that of AAO50 and AAO35. It is also 3.8 times higher than that of the 50 nm gold coated plain Si microcantilever with similar dimensions. This correspondence of simulated data and our experimental results successfully prove that increasing the pore diameter enhances the thermomechanical sensitivity of the AAO microcantilever. The thermomechanical sensitivities of AAO microcantilevers, especially AAO60, were much higher than other previously reported plain or nanoporous microcantilevers with different materials such as TiO_2 and Si. We further used and investigated the highly sensitive AAO60 for the detection of VOCs by using PCDS.

3.3 Detection of VOCs with AAO microcantilevers using PCDS

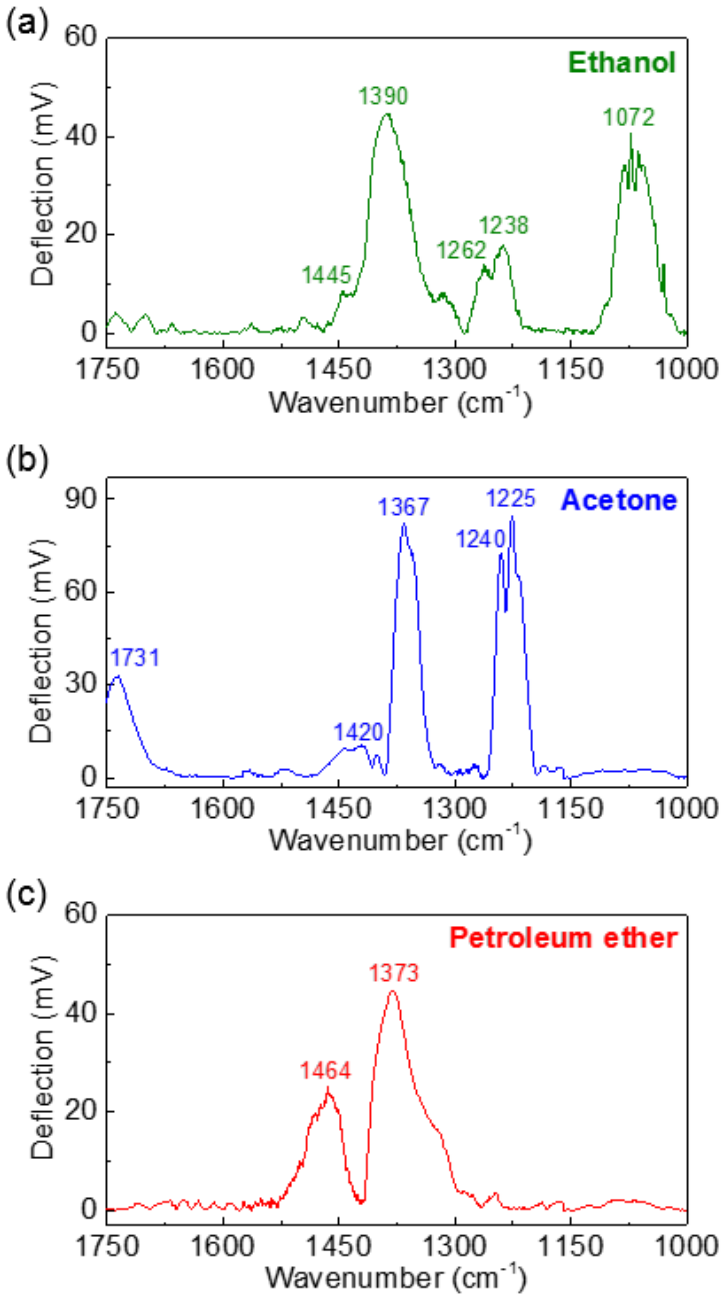

Figure 3.5. PCDS spectrum of (a) ethanol, (b) acetone, and (c) petroleum ether in a vapor phase based on AAO60 scanned with an IR range of 1750 cm^{-1} to 1000 cm^{-1}. The total flow rate was 100

sccm for all three cases. The concentration of ethanol, acetone and petroleum ether was 30 × 10^3 ppm, 15 ×10^3 ppm and 50 ×10^3 ppm, respectively.

Ethanol	
1445 cm^{-1}	Asymmetric CH_2 and CH_3 bending
1390 cm^{-1}	O-H bending
1238 cm^{-1}	Symmetric CH_2 bending
1072 cm^{-1}	C-O stretching
Acetone	
1737 cm^{-1}	C=O stretching
1420 cm^{-1}	Asymmetric CH_3 deformation
1367 cm^{-1}	Symmetric CH_3 deformation
1240 cm^{-1}	C-C vibration
1225 cm^{-1}	C-C vibration
Petroleum ether	
1464 cm^{-1}	CH_2 scissors vibration
1373 cm^{-1}	Symmetric deformation of CH_3 in aliphatic molecules

Table 3.1. Organic functional groups of ethanol, acetone, and petroleum ether molecules identified from PCDS spectrum by using AAO60.

Figure 3.5 shows the real-time PCDS spectrum of ethanol, acetone, and petroleum ether in a vapor phase by using nanoporous AAO60. A wide range of IR rom 1750 cm^{-1} to 1000 cm^{-1} was scanned in order to identify the various organic functional groups. They are analyzed through the PCDS spectrum using AAO60 as shown in Table 3.1. The PCDS spectra of ethanol (Figure 3.5a) clearly shows asymmetric CH_2 and CH_3 bending around 1445 cm^{-1}, O-H bending at 1390 cm^{-1}, symmetric CH_2 bending at 1238-1260 cm^{-1}, and C-O stretching at 1072 cm^{-1}. Figure 3.5b shows the PCDS spectra of acetone with C=O stretching at 1737 cm^{-1}, asymmetric CH_3 deformation at 1420 cm^{-1}, symmetric CH_3 deformation at 1367 cm^{-1}, and C-C vibrations at 1220-1240 cm^{-1}. CH_2 scissors vibration at 1464 cm^{-1} and symmetric deformation of CH_3 in aliphatic molecules at 1373 cm^{-1} of petroleum ether are also clearly shown in Figure 3.5c. They matched excellently with previously reported fourier transform infrared spectroscopy (FTIR) data[79 99 100]. PCDS has several advantages in detecting VOCs over FTIR such as small amount of sample needed and quick real-time measurement. The total scanning time of QCL IR between 1750 cm^{-1} to 1000 cm^{-1} took less than a minute.

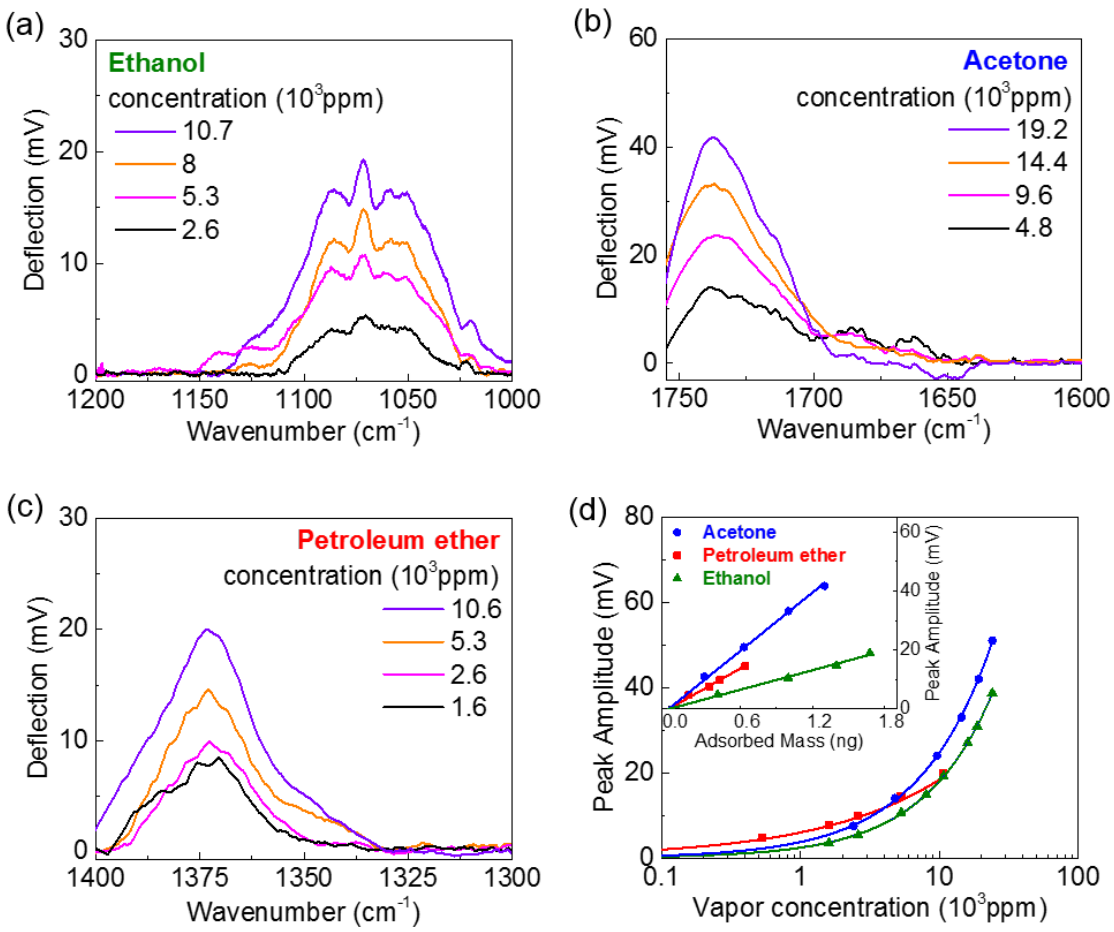

Figure 3.6. PCDS spectrum of (a) ethanol, (b) acetone, and (c) petroleum ether in a vapor phase at different concentrations by using AAO60. (d) IR peak amplitudes of ethanol at 1072 cm^{-1}, acetone at 1737 cm^{-1}, and petroleum ether at 1373 cm^{-1} as a function of vapor concentration and adsorbed mass. The Freundlich adsorption isotherm equation was used for fitting the peak amplitudes vs. vapor concentration curves.

In order to find the limit of detection (LOD) of ethanol, acetone, and petroleum ether by using PCDS with AAO60, we tested on various vapor concentrations of each organic vapor and measured the corresponding PCDS signals. Figure 3.6a-c show the PCDS spectra of ethanol, acetone, and petroleum ether with AAO60 at various vapor concentrations. The deflection

amplitudes around the peaks at 1737 cm^{-1} (C=O stretching) of acetone, 1072 cm^{-1} (C-O stretching) of ethanol and 1373 cm^{-1} (CH_3 deformation) of petroleum ether increase along with the increase in vapor concentration. More organic molecules are adsorbed on the AAO60 surface at a higher concentration, and they generate more heat under IR radiation. The IR peak amplitudes of ethanol (1072 cm^{-1}), acetone (1737 cm^{-1}), and petroleum ether (1373 cm^{-1}) are plotted as a function of a vapor concentration and adsorbed mass as shown in Figure 3.6d. The sensitivity of each organic vapor was calculated to be 11 mV/ng (ethanol), 33 mV/ng (acetone), and 23 mV/ng (petroleum ether), showing that the IR peak amplitudes are in direct proportions to the adsorbed mass. The LOD of organic molecules on AAO60 are estimated to be approximately 30.7 pg for ethanol, 8.3 pg for acetone, and 2.0 pg for petroleum ether, by tracing the intersection of the IR peak amplitudes as a function of adsorbed mass and the line with a standard deviation of 3. These LOD values in a picogram (10^{-12}) scale are due to the high thermomechanical sensitivity of AAO60.

IR peak amplitudes of the organic vapor molecules gradually increase with the vapor concentration; however, the slopes of fitting lines decrease as the vapor concentrations increase. This is because bare sites on the AAO surface are reduced as they are partially covered with previously attached molecules. The relations between IR peak amplitudes of the organic components and vapor concentrations were empirically found through the Freundlich adsorption isotherm equation

$$\frac{x}{m} = Kp^{1/n} \tag{6}$$

where x is the mass of adsorbate, m is the mass of adsorbent, p is the equilibrium pressure of adsorbate. K and n are the constants at a particular temperature. The limit of detection (LOD) for vapor concentrations of ethanol (1072 cm^{-1}), acetone (1737 cm^{-1}), and petroleum ether (1373 cm^{-}

[1]) are estimated to be approximately ~40 ppm, ~100 ppm ~25 ppm, respectively, by tracing the intersections of the adsorption isotherm fitting lines with IR peak amplitudes and the lines with standard deviation of 3. The disparate LOD value of each component is caused by the difference in QCL power, base signal and amount of atomic IR absorption at different wavenumbers. The power of the QCL at 1370 cm^{-1} is much higher than that of 1072 cm^{-1}. This makes the LOD of petroleum ether lower than that of ethanol, even though the affinity of ethanol on AAO surface is much higher than that of petroleum ether. From this result, we can expect that increasing the power of QCL can further enhance LOD in PCDS.

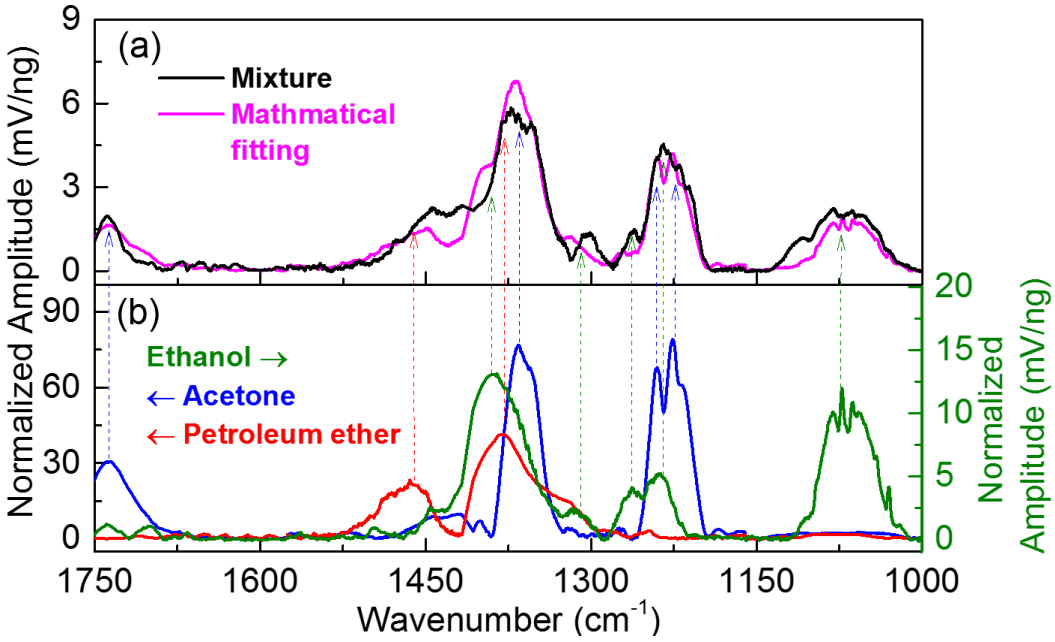

Figure 3.7. (a) Normalized PCDS spectra of the ternary mixture (black); ethanol, acetone and petroleum ether in humid condition, and the mathematical fitting (pink). (b) Normalized PCDS spectrum of ethanol (green), acetone (blue) and petroleum ether (red).

Figure 3.7b shows the normalized PCDS spectrum of ethanol (green), acetone (blue), and petroleum ether (red) in a wide IR range from 1750 cm^{-1} to 1000 cm^{-1}. The individual spectrum of each vapor was plotted as a reference. The adsorbed mass of ethanol, acetone, and petroleum ether on the AAO60 was calculated to be ~3.4 ng, 1.1 ng, and 1.1 ng at 53×10^3 ppm, 14.4×10^3 ppm and 29.3×10^3 ppm, respectively. The normalized IR spectrum were obtained by dividing the PCDS spectrum of the organic components by the adsorbed mass. Figure 3.7a shows the normalized IR spectra of the ternary vapor mixture in a humid condition (black) and the mathematical fitting (pink) with a weighted linear superposition of individual vapors IR spectra. Water vapor molecules (4.6×10^3 ppm, 20 % relative humidity) were mixed with the ternary mixture; ethanol at 29.3×10^3 ppm, acetone at 14.4×10^3 ppm, and petroleum ether at 53.3×10^3 ppm, to determine whether or not the humidity degrades the performance of the system. This was done since humidity is often very high in most environments such as an atmosphere, human breath, or an industrial site. Although some peaks were broad and low due to the peak convolutions in the spectrum, the unique molecular vibrational peaks were clearly observed in the normalized PCDS spectrum. In particular, the PCDS spectrum of the ternary vapor mixture clearly show C=O stretching of acetone (1737 cm^{-1}), C-O stretching of ethanol (1072 cm^{-1}), and CH_2 vibration and CH_3 deformation of petroleum ether (1464 cm^{-1} and at 1373 cm^{-1}). From these results, we could conclude that the PCDS technique based on the AAO microcantilever is capable of selectively and sensitively detecting individual organic components from vapor mixtures under humid conditions.

Although the concentrations of individual organic components from vapor mixtures inside the flow cell can be controlled, it is very hard to estimate the relative adsorbed mass of each component on sensor substrates. However, we could overcome this problem through the linear relation between the adsorbed mass and PCDS peak amplitudes. Total adsorbed mass of ternary

organic compounds and water molecules was calculated to be ~8.74 ng from tracing the resonance frequency shift. The PCDS spectra of the ternary mixture (black) was mathematically fitted (pink) to the combination of individual ethanol, acetone, and petroleum ether IR spectrum as shown in Figure 3.7a. The relative adsorbed mass was roughly estimated to be 1.69 ng (ethanol), 0.40 ng (acetone) and 0.32 ng (petroleum ether) from the mathematical fitting. The rest of the mass change would be due to the adsorption of water molecules. Small variations of the relative adsorbed mass ratio from single components and the mixture may be attributed to the competitive adsorption and their different molecular affinity to the AAO surface.

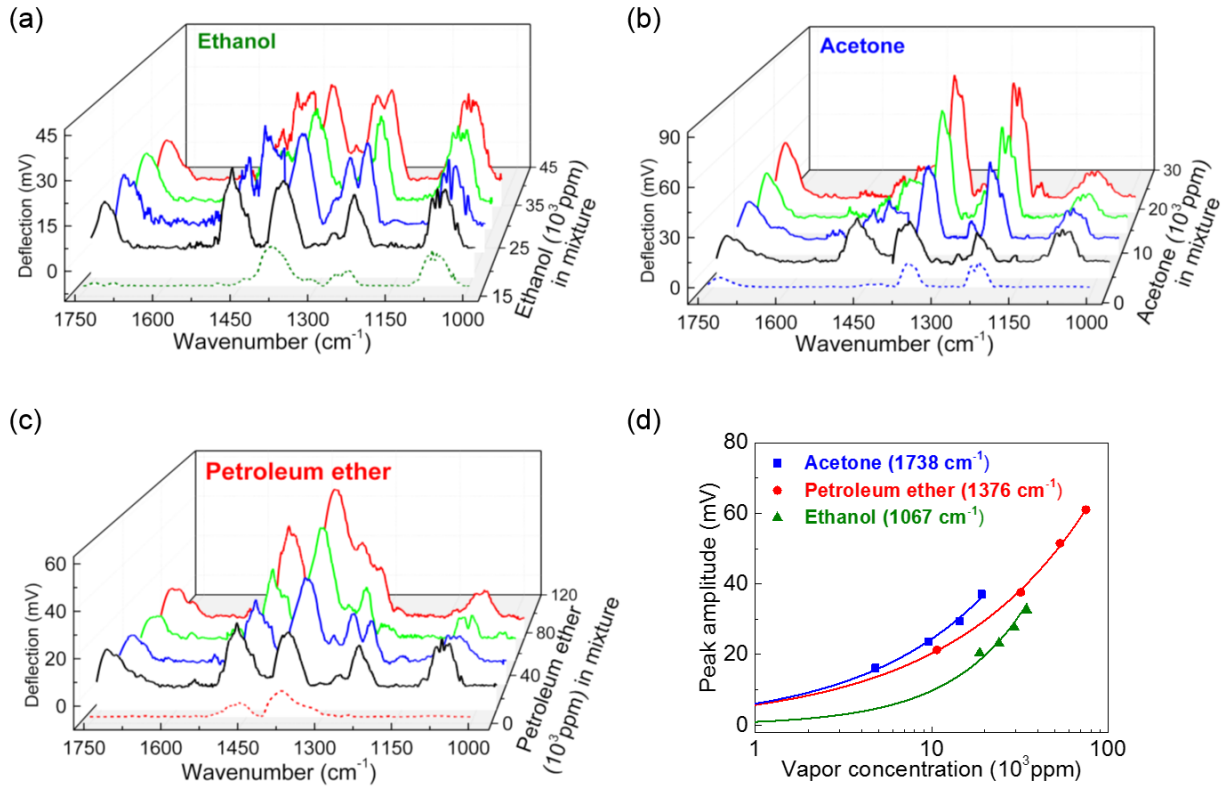

Figure 3.8. PCDS spectrum of ternary mixtures; ethanol, acetone, petroleum ether at 20 % relative humidity (RH) with increasing only (a) ethanol, (b) acetone and (c) petroleum ether concentrations from the ternary vapor mixture at fixed concentration (black). (d) Peak amplitudes of acetone at

1737 cm^{-1}, petroleum ether at 1373 cm^{-1} and ethanol at 1072 cm^{-1} as a function of vapor concentration in mixtures.

The maximum recognizable organic vapor mixture composition ranges from PCDS based on the nanoporous AAO microcantilever were estimated by measuring the limit of recognition (LOR). LOR is defined as the concentration of a target analyte below which the sensor cannot reliably recognize its response pattern to background molecules. LOR is expressed as the ratio of the target analyte to background molecules. In order to find the LOR of VOCs with our system, 12 PCDS spectra of vapor mixtures containing ethanol, acetone, and petroleum ether in humid conditions were obtained (Figure 3.8). Figure 3.8a shows the IR spectrum of ternary vapor mixtures (ethanol: acetone: petroleum ether = 18.6: 4.8: 10.6 $\times 10^3$ ppm) at 20 % RH with an increase in the concentration of only ethanol vapor from 18.6 to 34.6×10^3 ppm with the same vapor concentrations of acetone and petroleum ether. The PCDS spectrum of ethanol vapor (green dots) is presented as a reference. It is very hard to recognize which molecules are adsorbed or desorbed from the sensor surface by tracing the variations in the mass of AAO60. However, the PCDS spectrum clearly shows the increase of the ethanol peak areas from the ternary vapor mixtures when only ethanol concentration is increased. Little variations of the IR peak area from other vapors were observed due to the adsorption equilibrium induced by molecular affinity to the AAO surface. The actual mass adsorption of each component on AAO60 surface can be estimated by the mathematical fitting the same way as in Figure 3.7. The PCDS spectrum changes by increasing the vapor concentrations of only acetone and only petroleum ether (Figure 3.8b and Figure 3.8c) were also investigated with the same manner. The vapor concentrations of acetone and petroleum ether were increased from 4.8×10^3 ppm to 19.2×10^3 ppm and from 10.6×10^3 ppm

to 96.0×10^3 ppm, respectively, whereas the concentration of ethanol and relative humidity were kept constant.

The LOD of individual components from the ternary vapor mixtures were first measured to find the LOR. It is interesting to note that the LOD of the individual organic vapor molecules from the ternary mixtures were similar to the LOD of single organic vapors in Figure 3.6. The ratios of the target components' LOD to the concentrations of background molecules were calculated. These ratios are considered as the LOR of AAO60 in the PCDS system. They are estimated to be 1:250 of acetone to ethanol, 1:50 of ethanol to petroleum ether, and 1:100 of petroleum ether to acetone in ternary vapor mixtures at 20 % RH. These maximum recognizable mixture composition ranges of PCDS using AAO60 are far superior to those of previously reported methods.

Conclusion

We have identified and quantified the individual volatile organic molecules from vapor mixtures in humid condition by using a PCDS technique based on nanoporous AAO microcantilevers. By analyzing the variation in PCDS peak amplitudes of the specific molecular vibrations and resonance frequency shifts of AAO microcantilevers, we could sensitively and selectively detect ethanol, acetone, and petroleum ether molecules from their vapor mixtures. The thermomechanical sensitivity of AAO microcantilevers was enhanced by increasing their pore diameters, which also resulted in more adsorption of molecules with their higher surface areas. We were able to measure the adsorbed mass of individual organic components on the microcantilever surfaces from given ternary vapor mixtures under humid conditions. In addition, nanoporous AAO microcantilevers clearly showed the enhanced IR responses according to the increase in vapor concentrations of individual organic components from mixtures. With the results from this project, we can demonstrate that the PCDS combined with AAO microcantilevers can provide a highly sensitive and selective e-nose system for the detection of VOCs.

Future work

Future work will be focused on further increasing the sensitivity of PCDS with nanoporous AAO microcantilevers in order to detect VOCs at lower concentrations. We demonstrated the identification and quantification of VOCs vapor mixtures; however, the vapor concentrations which we have actually detected are still very high, compared to other methods such as using nanowires and metal oxide nanoprobes[11] [101]. Thus, we will try to increase the sensitivity by a functionalization of the AAO surface as it would increase the affinity of VOC molecules on the surface. Focusing IR with a lens to increase the intensity of mid IR can be another approach. Through these methods, we might be able to enhance the PCDS signals and lower the limits of detection. Also, we found that the AAO material itself absorbs a large amount of mid IR, and it generates noise from the base signal. We will coat a thin layer of gold, which does not absorb IR, on the AAO nanowells to reduce the noise. We expect to lower the limit of detection down to ppb concentration levels, and demonstrate that PCDS with nanoporous AAO microcantilevers can be used as a breath analysis tool. The higher relative humidity at 40 % and 60 % would be also tried in the future experiment to check if AAO microcantilever is properly working at higher humidity conditions.

Bibliography

1. CHEMICAL SENSORS DEFINITIONS AND CLASSIFICATION (IUPAC). at <http://pac.iupac.org/publications/pac/pdf/1991/pdf/6309x1247.pdf>

2. Sensitivity, Selectivity, and Stability of Gas-Sensitive Metal-Oxide Nanostructures. at <http://www.chem.msu.ru/rus/books/2011/sergeev/all.pdf>

3. Bandodkar, A. J. & Wang, J. Non-invasive wearable electrochemical sensors: a review. *Trends Biotechnol.* **32,** 363–71 (2014).

4. Viberg, M. & Ottersten, B. Sensor array processing based on subspace fitting. *IEEE Trans. Signal Process.* **39,** (1991).

5. Friedlander, B. A Sensitivity Analysis of the MUSIC Algorithm. *October* **38,** 1740–1751 (1990).

6. Vargas-Bernal, R. Techniques to optimize the selectivity of a gas sensor. *Electron. Robot. Automot. Mech. Conf. CERMA 2007 - Proc.* 579–584 (2007). doi:10.1109/CERMA.2007.4367749

7. Zellers, E. T., Park, J., Hsu, T. & Groves, W. A. Establishing a Limit of Recognition for a Vapor Sensor Array Organic vapor analysis with microsensor arrays relies principally on two output parameters : the response pattern , which provides qualitative information , and the. **70,** 4191–4201 (1998).

8. Sensors, Chemical Sensors, Electrochemical Sensors, and ECS. at <http://www.transducertech.com/media/ECS paperFNL.pdf>

9. Gardner, J. W., Shin, H. W. & Hines, E. L. An electronic nose system to diagnose illness. *Sensors Actuators B Chem.* **70,** 19–24 (2000).

10. Hill, D. & Binions, R. Breath Analysis for Medical Diagnosis. **5,** 401–440 (2012).

11. Wang, L., Kalyanasundaram, K., Stanacevic, M. & Gouma, P. Nanosensor Device for Breath Acetone Detection. *Sens. Lett.* **8,** 709–712 (2010).

12. Sensors for Agriculture and the Food Industry. at <http://www.electrochem.org/dl/interface/wtr/wtr10/wtr10_p041-046.pdf>

13. Adley, C. C. & Ryan, M. P. *High Throughput Screening for Food Safety Assessment*. *High Throughput Screen. Food Saf. Assess.* (Elsevier, 2015). doi:10.1016/B978-0-85709-801-6.00014-9

14. Di Francia, G., Alfano, B. & La Ferrara, V. Conductometric gas nanosensors. *J. Sensors* **2009,** (2009).

15. Chemical Sensors for Environmental Monitoring and Homeland Security. at <http://www.electrochem.org/dl/interface/wtr/wtr10/wtr10_p035-040.pdf>

16. Arshak, K., Moore, E., Lyons, G. M., Harris, J. & Clifford, S. A review of gas sensors employed in electronic nose applications. *Sens. Rev.* **24,** 181–198 (2004).

17. Polikar, R., Shinar, R., Honavar, V., Udpa, L. & Marc, D. Detection and identification of odorants using an electronic nose. 2–5

18. Baller, M. K. *et al.* A cantilever array-based artificial nose. *Ultramicroscopy* **82,** 1–9 (2000).

19. Purves, D. *et al.* The Organization of the Olfactory System. (2001). at <http://www.ncbi.nlm.nih.gov/books/NBK10982/>

20. DAMICO, A. *et al.* Olfactory systems for medical applications. *Sensors Actuators B Chem.* **130,** 458–465 (2008).

21. Electronic Nose and Olfactometry Article in R&D Magazine. at <http://www.fivesenses.com/rdmag.htm>

22. Choi, S.-J. *et al.* Selective diagnosis of diabetes using Pt-functionalized WO3 hemitube networks as a sensing layer of acetone in exhaled breath. *Anal. Chem.* **85,** 1792–6 (2013).

23. Röck, F., Barsan, N. & Weimar, U. Electronic Nose: Current Status and Future Trends. *Chem. Rev.* Published on the web, January 25 2008 DOI 10.1021/ (2008). doi:10.1021/cr068121q

24. Shurmer, H. V. & Gardner, J. W. Odour discrimination with an electronic nose. *Sensors Actuators B Chem.* **8,** 1–11 (1992).

25. *Handbook of Machine Olfaction*. (Wiley-VCH Verlag GmbH & Co. KGaA, 2002). doi:10.1002/3527601597

26. Sayago, I. *et al.* New sensitive layers for surface acoustic wave gas sensors based on polymer and carbon nanotube composites. *Procedia Eng.* **25,** 256–259 (2011).

27. Albert, K. J. *et al.* Cross-reactive chemical sensor arrays. *Chem. Rev.* **100,** 2595–626 (2000).

28. Muñoz, B. C., Steinthal, G. & Sunshine, S. Conductive polymer-carbon black composites-based sensor arrays for use in an electronic nose. *Sens. Rev.* **19,** 300–305 (1999).

29. Penza, M., Cassano, G., Sergi, A., Lo Sterzo, C. & Russo, M. . SAW chemical sensing using poly-ynes and organometallic polymer films. *Sensors Actuators B Chem.* **81,** 88–98 (2001).

30. Dai, G. A study of the sensing properties of thin film sensor to trimethylamine. *Sensors Actuators B Chem.* **53,** 8–12 (1998).

31. Schaller, E., Bosset, J. O. & Escher, F. 'Electronic Noses' and Their Application to Food. *LWT - Food Sci. Technol.* **31,** 305–316 (1998).

32. Albert, K. J. *et al.* Cross-Reactive Chemical Sensor Arrays. *Chem. Rev.* **100,** 2595–2626 (2000).

33. Carey, W. P. & Kowalski, B. R. Chemical piezoelectric sensor and sensor array characterization. *Anal. Chem.* **58,** 3077–3084 (1986).

34. Nagle, H. T., Gutierrez-Osuna, R. & Schiffman, S. S. The how and why of electronic noses. *IEEE Spectr.* **35,** 22–31 (1998).

35. Walt, D. R. *et al.* Optical sensor arrays for odor recognition. *Biosens. Bioelectron.* **13,** 697–699 (1998).

36. Lee, M. *et al.* Evaporation of water droplets from hydrophobic and hydrophilic nanoporous microcantilevers. *Appl. Phys. Lett.* **98,** 013107 (2011).

37. EUR-Lex - 32004L0042 - EN - EUR-Lex. at <http://eur-lex.europa.eu/legal-content/EN/ALL/;ELX_SESSIONID=3JvQJngSmHHt3xG8zQvgP7rpcbJBSBJhkfmLS1T1whtkt0hMpQ04!-722391354?uri=CELEX:32004L0042>

38. Goldstein, A. H. & Shaw, S. L. Isotopes of volatile organic compounds: an emerging approach for studying atmospheric budgets and chemistry. *Chem. Rev.* **103,** 5025–48 (2003).

39. Dales, R., Liu, L., Wheeler, A. J. & Gilbert, N. L. Quality of indoor residential air and health. *CMAJ* **179,** 147–52 (2008).

40. keyetv.com Austin News, Weather, Traffic KEYE-TV Austin :: News - Top Stories - DuPont Tragedy One Of Many Toxic Gas Releases. at <http://www.keyetv.com/news/features/top-stories/stories/dupont-tragedy-one-many-toxic-gas-releases-22388.shtml>

41. Irigaray, P. *et al.* Lifestyle-related factors and environmental agents causing cancer: an overview. *Biomed. Pharmacother.* **61,** 640–58 (2007).

42. Mazzone, P. J. Analysis of volatile organic compounds in the exhaled breath for the diagnosis of lung cancer. *J. Thorac. Oncol.* **3,** 774–80 (2008).

43. Oil Sands Tailings Pond - MicrobeWiki. at <https://microbewiki.kenyon.edu/index.php/Oil_Sands_Tailings_Pond>

44. Syncrude, Suncor cleared after duck death investigation - Calgary - CBC News. at <http://www.cbc.ca/news/canada/calgary/syncrude-suncor-cleared-after-duck-death-investigation-1.1271299>

45. Chaudhary, M. & Gupta, A. Microcantilever-based Sensors. *Def. Sci. J.* **59,** 634–641 (2009).

46. A Review of Microcantilevers for Sensing Applications. at <http://www.azonano.com/article.aspx?ArticleID=1927#_Abstract>

47. Loui, A. *et al.* Chemical vapor discrimination using a compact and low-power array of piezoresistive microcantilevers. *Analyst* **133,** 608–15 (2008).

48. Lee, D., Kim, S., Jeon, S. & Thundat, T. Direct detection and speciation of trace explosives using a nanoporous multifunctional microcantilever. *Anal. Chem.* **86,** 5077–82 (2014).

49. Krause, A. R., Van Neste, C., Senesac, L., Thundat, T. & Finot, E. Trace explosive detection using photothermal deflection spectroscopy. *J. Appl. Phys.* **103,** 094906 (2008).

50. Patil, S. J., Duragkar, N. & Rao, V. R. An ultra-sensitive piezoresistive polymer nano-composite microcantilever sensor electronic nose platform for explosive vapor detection. *Sensors Actuators, B Chem.* **192,** 444–451 (2014).

51. Cantilever Array Sensor Group. at <https://cantileversensors.unibas.ch/CLA/Welcome.html>

52. Pinnaduwage, L. A., Hawk, J. E., Boiadjiev, V., Yi, D. & Thundat, T. Use of Microcantilevers for the Monitoring of Molecular Binding to Self-Assembled Monolayers. *Langmuir* **19,** 7841–7844 (2003).

53. Pinnaduwage, L. A. *et al.* A sensitive, handheld vapor sensor based on microcantilevers. *Rev. Sci. Instrum.* **75,** 4554 (2004).

54. Zuo, G. *et al.* Dual-SAM functionalization on integrated cantilevers for specific trace-explosive sensing and non-specific adsorption suppression. *Nanotechnology* **18,** 255501 (2007).

55. Taylor, P., Thundat, T., Oden, P. I. & Warmack, R. J. Microscale Thermophysical Engineering MICROCANTILEVER SENSORS. 37–41 (2010).

56. Papadopoulos, C. A., Vlaehos, D. S. & Avaritsiotis, J. N. Comparative study of various metal-oxide-based gas-sensor architectures. **32,** (1996).

57. Datar, R. *et al.* C antilever Sensors : Nanomechanical Tools for Diagnostics. *MRS Bull.* **34,** 449–454 (2009).

58. Olcum, S. *et al.* Weighing nanoparticles in solution at the attogram scale. *Proc. Natl. Acad. Sci. U. S. A.* **111,** 1310–5 (2014).

59. Thundat, T., Warmack, R. J., Chen, G. Y. & Allison, D. P. Thermal and ambient-induced deflections of scanning force microscope cantilevers. *Appl. Phys. Lett.* **64,** 2894 (1994).

60. Dareing, D. W. & Thundat, T. Simulation of adsorption-induced stress of a microcantilever sensor. *J. Appl. Phys.* **97,** 043526 (2005).

61. Tamayo, J., Kosaka, P. M., Ruz, J. J., San Paulo, Á. & Calleja, M. Biosensors based on nanomechanical systems. *Chem. Soc. Rev.* **42,** 1287–311 (2013).

62. Micromanufacturing and Nanotechnology. at <http://download.springer.com/static/pdf/936/bfm%253A978-3-540-29339-2%252F1.pdf?auth66=1422506088_7195a55aea4b854f613161bc4d871b88&ext=.pdf>

63. Lavrik, N. V., Sepaniak, M. J. & Datskos, P. G. Cantilever transducers as a platform for chemical and biological sensors. *Rev. Sci. Instrum.* **75,** 2229 (2004).

64. Fritz, J. Cantilever biosensors. *Analyst* **133,** 855–63 (2008).

65. Meyer, G. & Amer, N. M. Novel optical approach to atomic force microscopy. *Appl. Phys. Lett.* **53,** 1045 (1988).

66. Sekaric, L., Carr, D. ., Evoy, S., Parpia, J. . & Craighead, H. . Nanomechanical resonant structures in silicon nitride: fabrication, operation and dissipation issues. *Sensors Actuators A Phys.* **101,** 215–219 (2002).

67. Thundat, T., Wachter, E. a., Sharp, S. L. & Warmack, R. J. Detection of mercury vapor using resonating microcantilevers. *Appl. Phys. Lett.* **66,** 1695 (1995).

68. Datskos, P. G. & Sauers, I. Detection of 2-mercaptoethanol using gold-coated micromachined cantilevers. *Sensors Actuators B Chem.* **61,** 75–82 (1999).

69. Lavrik, N. V., Sepaniak, M. J. & Datskos, P. G. Cantilever transducers as a platform for chemical and biological sensors. *Rev. Sci. Instrum.* **75,** 2229 (2004).

70. Naeli, K. & Brand, O. Cancellation of environmental effects in resonant mass sensors based on resonance mode and effective mass. *Rev. Sci. Instrum.* **80,** 063903 (2009).

71. Thundat, T., Chen, G. Y., Warmack, R. J., Allison, D. P. & Wachter, E. a. Vapor detection using resonating microcantilevers. *Anal. Chem.* **67,** 519–521 (1995).

72. Boisen, a., Thaysen, J., Jensenius, H. & Hansen, O. Environmental sensors based on micromachined cantilevers with integrated read-out. *Ultramicroscopy* **82,** 11–16 (2000).

73. Transactions, E. C. S. & Society, T. E. Photothermal Cantilever Deflection Spectroscopy Seonghwan Kim. **50,** 459–464 (2012).

74. Lee, D., Zandieh, O., Kim, S., Jeon, S. & Thundat, T. Sensitive and selective detection of hydrocarbon/water vapor mixtures with a nanoporous silicon microcantilever. *Sensors Actuators B Chem.* **206,** 84–89 (2015).

75. Covered, T. Application of AFM-IR Concept for Chemical Characterization of Organic Materials at Nanoscale Spatial Resolution. 1–6

76. Yun, M. *et al.* Photothermal cantilever deflection spectroscopy of a photosensitive polymer. *Appl. Phys. Lett.* **100,** 204103 (2012).

77. Sohi, A. N. & Nieva, P. M. Thermal sensitivity analysis of curved bi-material microcantilevers. *J. Micromechanics Microengineering* **24,** 115004 (2014).

78. Kim, S. *et al.* Molecular recognition using receptor-free nanomechanical infrared spectroscopy based on a quantum cascade laser. *Sci. Rep.* **3,** 1111 (2013).

79. Bagheri, M., Chae, I., Lee, D., Kim, S. & Thundat, T. Selective detection of physisorbed hydrocarbons using photothermal cantilever deflection spectroscopy. *Sensors Actuators B Chem.* **191,** 765–769 (2014).

80. Lee, D. *et al.* Enhanced mass sensitivity of ZnO nanorod-grown quartz crystal microbalances. *Sensors Actuators B Chem.* **135,** 444–448 (2009).

81. Lee, D. *et al.* Enhanced mass sensitivity of stress-free, silicon nanowire-grown microcantilever sensors. *Appl. Phys. Lett.* **90,** 113107 (2007).

82. Feng, E. H. & Jones, R. E. Carbon nanotube cantilevers for next-generation sensors. *Phys. Rev. B* **83,** 195412 (2011).

83. Lee, D., Shin, N., Lee, K.-H. & Jeon, S. Microcantilevers with nanowells as moisture sensors. *Sensors Actuators B Chem.* **137,** 561–565 (2009).

84. Ono, S., Saito, M., Ishiguro, M. & Asoh, H. Controlling Factor of Self-Ordering of Anodic Porous Alumina. *J. Electrochem. Soc.* **151,** B473 (2004).

85. Dai, Z. & Ju, H. Bioanalysis based on nanoporous materials. *TrAC Trends Anal. Chem.* **39,** 149–162 (2012).

86. Santos, A., Kumeria, T. & Losic, D. Nanoporous anodic aluminum oxide for chemical sensing and biosensors. *TrAC Trends Anal. Chem.* **44,** 25–38 (2013).

87. Van Neste, C. W., Senesac, L. R. & Thundat, T. Standoff spectroscopy of surface adsorbed chemicals. *Anal. Chem.* **81,** 1952–6 (2009).

88. Md Jani, A. M., Losic, D. & Voelcker, N. H. Nanoporous anodic aluminium oxide: Advances in surface engineering and emerging applications. *Prog. Mater. Sci.* **58,** 636–704 (2013).

89. Lee, W., Nielsch, K. & Gösele, U. Self-ordering behavior of nanoporous anodic aluminum oxide (AAO) in malonic acid anodization. *Nanotechnology* **18,** 475713 (2007).

90. Wernick, S., Pinner, R. & Sheasby, P. G. *The surface treatment and finishing of aluminium and its alloys, Volume 2*. (ASM International, 1987). at <http://books.google.ca/books/about/The_surface_treatment_and_finishing_of_a.html?id=3vlTAAAAMAAJ&pgis=1>

91. Lee, W., Ji, R., Gösele, U. & Nielsch, K. Fast fabrication of long-range ordered porous alumina membranes by hard anodization. *Nat. Mater.* **5,** 741–7 (2006).

92. Abd-elnaiem, A. M. & Gaber, A. Parametric Study on the Anodization of Pure Aluminum Thin Film Used in Fabricating Nano-pores Template. **8,** 9741–9751 (2013).

93. Lee, P. S. *et al.* Microcantilevers with nanochannels. *Adv. Mater.* **20,** 1732–1737 (2008).

94. Lee, D. *et al.* Photoacoustic spectroscopy of surface adsorbed molecules using a nanostructured coupled resonator array. *Nanotechnology* **25,** 035501 (2014).

95. Yim, C. *et al.* Nanomechanical Thermal Analysis of Indium Films Using Silicon Microcantilevers. *Jpn. J. Appl. Phys.* **51,** 08KB07 (2012).

96. Tseytlin, Y. M. High resonant mass sensor evaluation: An effective method. *Rev. Sci. Instrum.* **76,** 115101 (2005).

97. Wasisto, H. S. *et al.* Airborne engineered nanoparticle mass sensor based on a silicon resonant cantilever. *Sensors Actuators B Chem.* **180,** 77–89 (2013).

98. Mutalib Md Jani, A. *et al.* Nanoporous anodic aluminium oxide membranes with layered surface chemistry. *Chem. Commun. (Camb).* 3062–4 (2009). doi:10.1039/b901745c

99. Zhang, X. K., Lewars, E. G., Raymond, E. & Pads, J. M. Vibrational Spectrum of the Acetone-Water Complex : A Matrix Isolation FTIR and Theoretical Study. 4320–4325 (1993).

100. Plyler, E. K. Infrared spectra of methanol, ethanol, and n-propanol. *J. Res. Natl. Bur. Stand. (1934).* **48,** 281 (1952).

101. Cao, A., Sudhölter, E. J. R. & de Smet, L. C. P. M. Silicon nanowire-based devices for gas-phase sensing. *Sensors (Basel).* **14,** 245–71 (2013).